# Second Harmonic Generation in Silicon Photonic Crystal Resonators for Quantum Optic Applications

by

H. Azzouz

B.S.E.E., Purdue University (2019)

Submitted to the Department of Electrical Engineering and Computer Science
in partial fulfillment of the requirements for the degree of

Master of Science

at the

MASSACHUSETTS INSTITUTE OF TECHNOLOGY

February 2023

Authored by: . . . . . . . . . . . . . . . . . . . . . . . . . . . . . . . . . . . . . . . . . . . . . . . . . . . . . . . . . . . . .
H. Azzouz
Department of Electrical Engineering and Computer Science
January 20, 2023

Certified by . . . . . . . . . . . . . . . . . . . . . . . . . . . . . . . . . . . . . . . . . . . . . . . . . . . . . . . . . . . . . .
Dirk R. Englund
Associate Professor of Electrical Engineering and Computer Science
Thesis Supervisor

Accepted by . . . . . . . . . . . . . . . . . . . . . . . . . . . . . . . . . . . . . . . . . . . . . . . . . . . . . . . . . . . . .
Leslie A. Kolodziejski
Professor of Electrical Engineering and Computer Science
Chair, Department Committee on Graduate Students

# Second Harmonic Generation in Silicon Photonic Crystal Resonators for Quantum Optic Applications

by

H. Azzouz

Submitted to the Department of Electrical Engineering and Computer Science
on January 20, 2023, in partial fulfillment of the
requirements for the degree of
Master of Science

## Abstract

A possible way of achieving all-photonic classical and quantum logic gates is with dynamically coupled photonic crystal cavities. A silicon architecture that has octave-separated resonances with high quality factor, low mode volume, high nonlinear coupling is implemented in the form of a one dimensional photonic crystal nanobeam cavity for efficient second harmonic generation.

Thesis Supervisor: Dirk R. Englund
Title: Associate Professor of Electrical Engineering and Computer Science

# Acknowledgments

I would like to first thank my research advisor, Professor Dirk Englund. He is deeply enthusiastic about advancing the frontiers of quantum science and photonic engineering and always has sharp insights and suggestions about research. I had many great discussions with Dirk about my research projects. His encouragement and great ideas have been critical to the success of this work.

I would like to next express my gratitude to my research mentor, Dr. Mikkel Heuck, for his extensive help throughout my research journey. He is always happy to meet with me and has kindly spent many hours explaining theory and simulation techniques, which I will always appreciate. I have learned greatly from Mikkel's deep understanding of photonics and his invaluable research expertise and advice.

I would like to acknowledge the QP-Group for upkeeping and supporting access to the Lumerical and Comsol servers. Also, I would like to acknowledge the EECS Graduate Office, especially Professor Leslie Kolodziejski and Janet Fischer, for keeping in touch and ensuring that my graduate experience runs smoothly.

Most importantly, I want to express my biggest thank you to my Mother and Father for their never ending love, support, teaching, advice, and guidance over my entire life. My research journey would not have been possible if it weren't for them. Last but not least, I want to say thank you to my Sister and Brother for always being there for me and for having many fun conversations about science and electrical engineering.

THIS PAGE INTENTIONALLY LEFT BLANK

# Contents

**1 Introduction 13**

1.1 Electric Field-Induced Second Harmonic Generation . . . . . . . . . . 14

1.2 Second Harmonic Generation Formalism . . . . . . . . . . . . . . . . 16

1.3 Photonic Crystal Cavities . . . . . . . . . . . . . . . . . . . . . . . 18

1.4 Design Objectives . . . . . . . . . . . . . . . . . . . . . . . . . . . 20

**2 Geometric Setup & Unit Cell Design for Octave-Separated Bandgaps 23**

2.1 Photonic Crystal Unit Cell Geometry . . . . . . . . . . . . . . . . . 23

2.2 MPB Simulation Setup . . . . . . . . . . . . . . . . . . . . . . . . . 24

2.3 Final Band Diagram Results . . . . . . . . . . . . . . . . . . . . . . 26

**3 Photonic Crystal Cavity Design Approach 29**

3.1 Recipe for Deterministic Design of Ultra-High $Q$-Factor Microcavities 29

3.2 Design of Cavity Tapering Profile . . . . . . . . . . . . . . . . . . . 30

3.3 Electrode Geometry . . . . . . . . . . . . . . . . . . . . . . . . . . 34

3.4 LUMERICAL FDTD Simulation Setup . . . . . . . . . . . . . . . . . 35

3.5 LUMERICAL FDTD Gridding . . . . . . . . . . . . . . . . . . . . . 37

3.6 Total Quality Factors . . . . . . . . . . . . . . . . . . . . . . . . . . 38

3.7 Radiative Quality Factors . . . . . . . . . . . . . . . . . . . . . . . 39

3.8 Mode Profiles and Overlap . . . . . . . . . . . . . . . . . . . . . . . 41

3.9 COMSOL FEM Simulation . . . . . . . . . . . . . . . . . . . . . . . 44

3.10 Extension of Second Harmonic Generation Formalism . . . . . . . . . 45

3.11 Effective Second-Order Nonlinearity . . . . . . . . . . . . . . . . . . 46

3.12 Resulting Figures of Merit . . . . . . . . . . . . . . . . . . . . . . . . . 48

**4 Cavity Length Optimization** **49**

4.1 Simulation Approach for Enhancing SHG Efficiency Per Power . . . . 49

4.2 Results of Sweep on Unit Cell Count . . . . . . . . . . . . . . . . . . 50

4.3 Figures of Merit Summary . . . . . . . . . . . . . . . . . . . . . . . . . 51

**5 Conclusions** **55**

# List of Figures

1-1 The left panel depicts a general second-harmonic generation system. The right panel illustrates the corresponding energy level diagram. Copied from [11]. . . . . . . . . . . . . . . . . . . . . . . . . . . . 15

1-2 (a) *Left Panel:* Band structure for infinite planar dielectric waveguide. (b) *Right Panel:* Band structure for infinite periodic planar dielectric waveguide. Copied from [15]. . . . . . . . . . . . . . . . . . . . . . . . . 19

2-1 3D rendering of the silicon 1D photonic crystal device concept. . . . . 24

2-2 1D photonic crystal band structure result. . . . . . . . . . . . . . . . 27

3-1 (a) *Top:* Final nonlinear $r_x(p)$, $r_y(p)$ tapering profile. (b) *Bottom:* Final linear $M_{1_{act}}(p)$, $M_{2_{act}}(p)$ mirror strength profiles for the first and second harmonic modes. . . . . . . . . . . . . . . . . . . . . . . . . 33

3-2 LUMERICAL illustration of symmetry conditions and source positioning. The device geometry is not rendered to scale. . . . . . . . . . . 35

3-3 (a) *Left:* Uniform LUMERICAL $X-$mesh. (b) *Center:* Nonuniform LUMERICAL $Y-$mesh. (c) *Right:* Nonuniform LUMERICAL $Z-$mesh. 38

3-4 *Left Column:* First Harmonic (a-i) Transmitted power, (a-ii) Radiated power, (a-iii) Total power leaving simulation domain. *Right Column:* Second Harmonic (b-i) Transmitted power, (b-ii) Radiated power, (b-iii) Total power leaving simulation domain. . . . . . . . . . . . . . . 40

3-5 (a) $xy-$cross section of the fundamental mode. (b) $xz-$cross section of the fundamental mode. (c) $xy-$cross section of the second harmonic mode. (d) $xz-$cross section of the second harmonic mode. . . . . . . 42

3-6 (a) *Top:* $xy-$cross section, and (b) *Bottom:* $xz-$cross section, of the optical field overlap used as a factor of the integrand in the numerator of $\bar{\beta}$. . . . . . . . . . . . . . . . . . . . . . . . . . . . . . . . . . . 43
3-7 Spatially alternating DC field [V/m]. . . . . . . . . . . . . . . . . . . 44
3-8 (a) *Top:* $\chi^{(2)}_{induced}$ over the selected $x-$integration region. (b) *Bottom:* Variation in the volumetric average $\overline{\chi}^{(2)}_{\text{effective}}$ as a function of symmetric $x-$integration range. . . . . . . . . . . . . . . . . . . . . . . . . . . . 47

4-1 (a) *Top:* Total and radiative quality factors, and (b) *Bottom:* Ratios of total to radiative quality factors, as a function of nanobeam size for both the first and second harmonics. . . . . . . . . . . . . . . . . . . . . 53
4-2 (a) *Top:* Device figure of merit 2, and (b) *Bottom:* Device figure of merit 1, as a function of nanobeam size. . . . . . . . . . . . . . . . . 54

# List of Tables

2.1 Geometric parameters of the photonic crystal unit cell and their corresponding definitions. . . . . . . . . . . . . . . . . . . . . . . . . . . . 25

2.2 Numerical design values for unit cell parameters in normalized and SI units. . . . . . . . . . . . . . . . . . . . . . . . . . . . . . . . . . 26

3.1 Fundamental and second harmonic resonant frequencies and their corresponding total quality factors $Q_1$ and $Q_2$. . . . . . . . . . . . . . . . 39

3.2 Transmitted, radiated, and total quality factors for the fundamental and second harmonic modes. . . . . . . . . . . . . . . . . . . . . . . . 41

3.3 Comparison of achieved Figures of Merit (FOMs) with preexisting designs in the literature. Note that the micropost design and this work's silicon microcavity design are only simulated whereas the GaAs microcavity design is also experimentally verified. . . . . . . . . . . . . . . 48

4.1 Updated transmitted, radiated, and total quality factors for the fundamental and second harmonic modes. . . . . . . . . . . . . . . . . . 52

4.2 Comparison of optimized Figures of Merit (FOMs) with preexisting designs in the literature. Note that the micropost design and this work's silicon microcavity design are only simulated whereas the GaAs microcavity design is also experimentally verified. . . . . . . . . . . 52

5.1 Estimates of effective second-order nonlinearities achievable with different applied electrode bias voltages. $E_{dc,y}^{eff}$ is estimated using $\overline{\chi}^{(2)}_{\text{effective}} = 3\chi^{(3)}E_{dc,y}^{eff}$. . . . . . . . . . . . . . . . . . . . . . . . . . . . . . . 56

THIS PAGE INTENTIONALLY LEFT BLANK

# Chapter 1

# Introduction

Controlling complex quantum mechanical systems at room temperature remains a central driving force in quantum information science. In the area of quantum computing, these efforts have largely focused on photonic quantum systems, progressing toward the long term goal of making a scalable, room temperature, photonic, quantum processor. A proposed way of achieving photon-photon quantum logic gates is with dynamically coupled photonic crystal cavities. Theoretical work has shown that at room temperature with bulk second-order optical nonlinearities, near-unity gate fidelity can be achieved by the capture and release of photonic qubits in dynamically coupled nanocavities [1, 2].

Furthermore, two multimode programmable photonic resonators are sufficient for realizing a complete photonic quantum error correction circuit [3]. Second harmonic generation inside a multimode cavity is also a critical prerequisite for obtaining deterministic high fidelity quantum controlled-phase gates based on dynamically coupling photons to a two-level emitter [4]. Additionally, recent simulation work has demonstrated the possibility of using nonlinear optics to build an all-photonic artificial neural network processor that can directly represent negative and complex numbers [5]. More generally, efficient second harmonic generation on photonic chips is important for applications like telecommunications, single-photon blockades, metrology, biosensing, converting infrared light to visible light for imaging, and basic quantum science research. High-performance photonic crystal microcavities are a promising approach for achieving low energy, high-bandwidth all-optical switches [6, 7] and can also be used for intrinsically forming neuron action potential-like signals [8].

In this thesis, a mechanism is introduced for achieving high nonlinear coupling rates in silicon for second harmonic generation. Specifically, this work proposes a controllable one-dimensional photonic crystal nanobeam microcavity design in silicon that can realize high quality factors with small interaction mode volumes. Spatially periodic DC electric fields are applied across the cavity to provide active controllability and to obtain an induced [9, 10] second-order nonlinear susceptibility $\chi^{(2)}$ from silicon's third-order nonlinearity $\chi^{(3)}$. This approach will enable a wide range of quantum and classical applications, including presenting a potential pathway toward scalable room temperature compatible photon-photon quantum logic gates and all-optical switches and transistors.

## 1.1 Electric Field-Induced Second Harmonic Generation

From [11], an applied optical field at a single frequency $\omega$, $E(t) \propto e^{i\omega t}$, incident on an arbitrary nonlinear, dispersionless, isotropic medium, induces a polarization response $P(t)$ given by

$$\begin{aligned} P(t) &\equiv P^{(1)}(t) + P^{(2)}(t) + P^{(3)}(t) + \dots && (1.1) \\ &= \varepsilon_0 \chi^{(1)} E(t) + \varepsilon_0 \chi^{(2)} E^2(t) + \varepsilon_0 \chi^{(3)} E^3(t) + \dots && (1.2) \end{aligned}$$

where $\varepsilon_0$ is the permittivity of free space, $\chi^{(1)}$ is the linear susceptibility, $\chi^{(2)}$ is the second-order nonlinearity, $\chi^{(3)}$ is the third-order nonlinear susceptibility, and so on. If the medium was anisotropic, the scalar susceptibilities would be replaced by tensors, and if the medium had dispersion (and losses), then according to the Kramers-Kronig relations, the polarization response would not be instantaneous.

In second-harmonic generation (SHG), an electromagnetic wave is incident on a material with non-zero second-order susceptibility. This causes the output wave to have components at both the incident frequency and at double the incident frequency, as seen in Fig. 1-1.

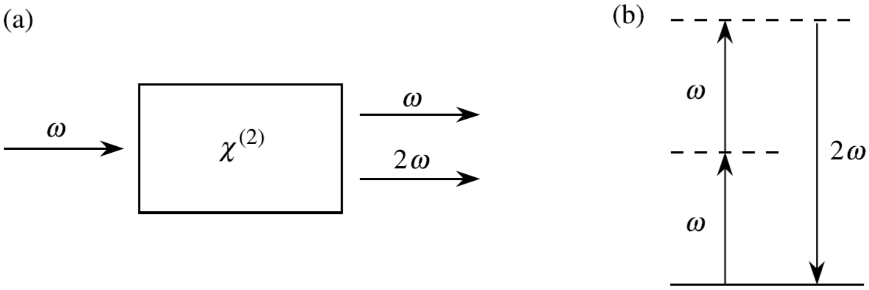

Figure 1-1: The left panel depicts a general second-harmonic generation system. The right panel illustrates the corresponding energy level diagram. Copied from [11].

For an incident electric field $E(t) = A\cos(\omega t)$, substituting into Eq. (1.2) gives

$$\begin{aligned} P(t) &= \varepsilon_0\chi^{(1)}A\cos(\omega t) + \varepsilon_0\chi^{(2)}A^2\cos^2(\omega t) \\ &= \underbrace{\frac{1}{2}\varepsilon_0\chi^{(2)}A^2}_{\text{DC Component}} + \underbrace{\varepsilon_0\chi^{(1)}A\cos(\omega t)}_{\text{Fundamental Component}} + \underbrace{\frac{1}{2}\varepsilon_0\chi^{(2)}A^2\cos(2\omega t)}_{\text{Second Harmonic Component}} \end{aligned} \tag{1.3}$$

From a practical standpoint, the maturity of complementary metal-oxide semiconductor (CMOS) fabrication processes makes using materials such as silicon, silicon nitride, or silicon dioxide attractive choices for building scalable photonic devices in applications such as machine learning accelerators and quantum computing architectures. Additionally, recent advances in wafer-scale nanofabrication of telecom single-photon emitters in silicon [12] make it a promising platform for scaling up quantum photonic integrated circuits to millions of qubits.

However these materials are centrosymmetric, and thus their second-order nonlinear susceptibility $\chi^{(2)}$ is negligible. Ref. [9] theoretically and experimentally demonstrates that applying a DC electric field across silicon breaks the crystalline symmetry and allows silicon's third-order nonlinearity $\chi^{(3)}$ to be converted into a second-order nonlinear susceptibility $\chi^{(2)}$. This can be advantageous for applications such as ultrafast nonlinear electro-optical sampling [13] that require background-free controllability, since turning off the DC field corresponds to completely removing the SHG signal.

Based on Refs. [9, 10], electric-field-induced second-harmonic (EFISH) generation can be derived as follows. Let the total electric field in a region of silicon, $E_{tot}(t)$, have a DC component, $E_{dc}$, and an optical component $E_\omega(t)$ at frequency $\omega$. Substituting $E_{tot}(t) = E_{dc} + E_\omega(t)$ into Eq. (1.2) yields

$$\begin{aligned}
P(t) &= \varepsilon_0 \chi^{(1)} E_{tot}(t) + \varepsilon_0 \cancelto{\text{0 for Si}}{\chi^{(2)}} E_{tot}^2(t) + \varepsilon_0 \chi^{(3)} E_{tot}^3(t) \\
&= \varepsilon_0 \left[ \chi^{(1)} \left( E_{dc} + E_\omega(t) \right) + \chi^{(3)} \left( E_{dc} + E_\omega(t) \right)^3 \right] \\
&= \varepsilon_0 \left[ \chi^{(1)} \left( E_{dc} + E_\omega(t) \right) + \chi^{(3)} \left( E_{dc}^3 + E_\omega^3(t) + 3E_{dc}^2 E_\omega(t) + 3E_{dc} E_\omega^2(t) \right) \right] \\
&= \varepsilon_0 \Big[ \underbrace{\left\{ \chi^{(1)} E_{dc} + \chi^{(3)} E_{dc}^3 \right\}}_{\text{DC Offset}} + \underbrace{\left\{ \chi^{(1)} + 3\chi^{(3)} E_{dc}^2 \right\}}_{\chi^{(1)}_{\text{effective}}} E_\omega(t) \\
&\qquad + \underbrace{\left\{ 3\chi^{(3)} E_{dc} \right\}}_{\chi^{(2)}_{\text{induced}}} E_\omega^2(t) + \underbrace{\left\{ \chi^{(3)} \right\}}_{\chi^{(3)}} E_\omega^3(t) \Big] \\
\therefore &\quad \boxed{\chi^{(2)}_{\text{induced}} = 3\chi^{(3)} E_{dc}} \qquad (1.4)
\end{aligned}$$

Eq. (1.4) shows that a DC applied E-field can induce a second-order nonlinear susceptibility $\chi^{(2)}$ from a third-order nonlinear susceptibility $\chi^{(3)}$. Following Refs. [9, 10], this work uses $\chi^{(3)} \approx 2.45 \times 10^{-19}$ m$^2$ V$^{-2}$, which corresponds to telecom wavelengths $\lambda \approx 1.55$ $\mu$m in silicon.

## 1.2 Second Harmonic Generation Formalism

For this thesis, it is sufficient to consider the case of a simple diagonal second order nonlinearity tensor. Ref. [14] defines the relevant figures of merit for quantifying and comparing designs for second-harmonic generation as follows:

Let $\varepsilon_1$ and $\varepsilon_2$ be the relative permittivities of the material at the first $(f_1, \lambda_1)$ and second $(f_2, \lambda_2)$ harmonics, respectively. Let $\bar{\varepsilon}(\vec{\boldsymbol{r}})$ be an indicator function that is 1 at positions with nonlinear material and 0 elsewhere. Additionally, let $\vec{\boldsymbol{E}}_1(\vec{\boldsymbol{r}})$ and $\vec{\boldsymbol{E}}_2(\vec{\boldsymbol{r}})$ be the electric fields of the first and second harmonic modes. Lastly, let the

$y$ direction align with the orientation of the nonlinear material's crystal axis. The dimensionless nonlinear coupling coefficient $\bar{\beta}$ is then defined by Ref. [14] as

$$\bar{\beta} = \frac{\displaystyle\int \bar{\varepsilon}(\vec{\boldsymbol{r}}) E_{1_y}^2 E_{2_y}^* \ d^3\vec{\boldsymbol{r}}}{\left(\displaystyle\int \varepsilon_1 |\vec{\boldsymbol{E}}_1|^2 \ d^3\vec{\boldsymbol{r}}\right)\left(\sqrt{\displaystyle\int \varepsilon_2 |\vec{\boldsymbol{E}}_2|^2 \ d^3\vec{\boldsymbol{r}}}\right)} \sqrt{\lambda_1^3} \tag{1.5}$$

Let $Q_1$ and $Q_2$ be the total (dimensionless) quality factors, let $Q_1^{rad}$ and $Q_2^{rad}$ be the radiative quality factors, and let $Q_1^{tra}$ and $Q_2^{tra}$ be the transmission coupling quality factors corresponding to the fundamental and second harmonic modes, respectively. Neglecting material absorption, total quality factors are

$$Q_{1,2} = \frac{1}{\frac{1}{Q_{1,2}^{rad}} + \frac{1}{Q_{1,2}^{tra}}} \tag{1.6}$$

The transmissions at the cavity resonant frequencies are [15]

$$\begin{aligned} T_{1,2} &= \left(\frac{Q_{1,2}}{Q_{1,2}^{tra}}\right)^2 && (1.7) \\ &= \left(1 - \frac{Q_{1,2}}{Q_{1,2}^{rad}}\right)^2 && (1.8) \end{aligned}$$

The dimensionless efficiency per power is given by the first figure of merit

$$\begin{aligned} \text{FOM}_1 &= Q_1^2 Q_2 |\bar{\beta}|^2 \left(1 - \frac{Q_1}{Q_1^{rad}}\right)^2 \left(1 - \frac{Q_2}{Q_2^{rad}}\right) && (1.9) \\ &= Q_1^2 Q_2 |\bar{\beta}|^2 T_1 \sqrt{T_2} && (1.10) \end{aligned}$$

For a given pair of intrinsic radiative lifetimes $Q_1^{rad}$, $Q_2^{rad}$ this figure of merit is maximized when $Q_1/Q_1^{rad} = Q_2/Q_2^{rad} = 0.5$, which can be easily verified. This corresponds to critical coupling of the first and second harmonic modes.

The dimensionless intrinsic upper bound on efficiency per power is quantified by the second figure of merit

$$\text{FOM}_2 = \left(Q_1^{rad}\right)^2 Q_2^{rad} |\bar{\beta}|^2 \tag{1.11}$$

When the first and second harmonic modes are critically coupled, $\mathrm{FOM}_1 = \mathrm{FOM}_1^{max} = \mathrm{FOM}_2/64$. Furthermore, both figures of merit improve proportionally with the squared magnitude of the normalized nonlinear coupling $\bar{\beta}$.

## 1.3 Photonic Crystal Cavities

Atomic and molecular crystals are periodic arrangements of atoms or molecules within a lattice. Electrons propagating through these crystals encounter a periodic potential. This lattice potential allows electrons of some energy levels to propagate through the crystal lattice, while electrons of certain other energy levels within band gaps of the dispersion relation are prevented from propagating in certain directions.

Photonic crystals are the optical equivalent of atomic and molecular crystals [15]. In photonic crystals, the electrons are replaced by photons, the atoms and molecules are replaced by patterned dielectric materials, and a periodic dielectric function takes on the role of the periodic atomic potential. The photonic dispersion relation, also known as a band structure or diagram, contains optical band gaps that obstruct the propagation of light with certain frequencies and polarizations in certain directions. These concepts can be used to control the propagation of light to yield high-$Q$ photonic resonances.

In general, band structures are plots of the allowable frequencies of eigenmode solutions of Maxwell's Equations versus the component of the wave vector that is parallel to the dielectric interface. This is illustrated in Fig. 1-2(a) for an infinite planar dielectric waveguide. The modes of this waveguide can be categorized as either guided modes or unguided modes. Unguided modes are also termed radiation modes or extended states. Propagation in free space is governed by the dispersion relation $\omega = c|\vec{\boldsymbol{k}}| = c\sqrt{k_{\parallel}^2 + k_{\perp}^2}$. The red light-line in Fig. 1-2(a) is $\omega = ck_{\parallel}$ which corresponds to $k_{\perp} = 0$. For a fixed $k_{\parallel}$, since $k_{\perp}$ can take on any value to satisfy the dispersion relation for an arbitrarily high $\omega > ck_{\parallel}$, there is a continuum of extended states above the light line. These extended states form the light cone.

Solving Maxwell's equations also yields a discrete set of guided modes underneath the light line, which are localized to the waveguide. These localized modes can be viewed as total internal reflected (TIR) modes. The corresponding dispersion curves asymptotically approach the line $\omega = \frac{c}{n}k_{\parallel}$ as $k_{\parallel}$ becomes large, where $n$ is the refractive index inside the waveguide [16].

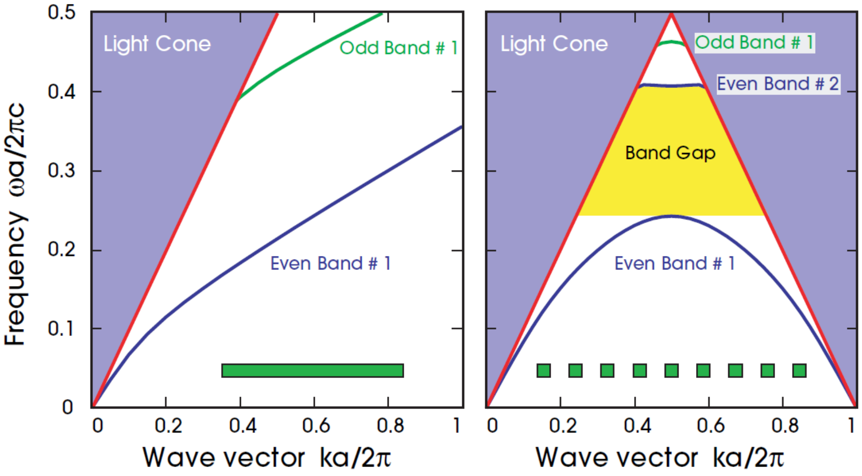

Figure 1-2: (a) *Left Panel:* Band structure for infinite planar dielectric waveguide. (b) *Right Panel:* Band structure for infinite periodic planar dielectric waveguide. Copied from [15].

On the other hand, Fig. 1-2(b) depicts the dispersion relation of an infinite planar periodic dielectric. This 1D photonic crystal is a repetition of its fundamental block, known as a unit cell. Let $a$ be the length of the unit cell in the direction of propagation. Bloch's Theorem states that the guided mode solutions are of the form $e^{i\vec{\boldsymbol{k}}\cdot\vec{\boldsymbol{r}}}$ multiplied by a unit cell function $\vec{\boldsymbol{u}}_k(\vec{\boldsymbol{r}})$ with period equal to the lattice vector $\vec{\boldsymbol{R}}$. For a 1D photonic crystal, as a consequence of Bloch's Theorem, only $k_{\parallel}$ in a range of length $\frac{2\pi}{a}$ is unique. Therefore, only the Brillouin zone $0 < k_{\parallel} \leq \frac{2\pi}{a}$ needs to be considered to characterize the guided solutions for all $k_{\parallel}$.

Furthermore, symmetries within the 1D photonic crystal unit cell lead to corresponding symmetries within the Brillouin zone. The irreducible Brillouin zone is the smallest subsection of the Brillouin zone that does not contain any symmetry relations. In Fig. 1-2(b), the irreducible Brillouin zone is $0 < k_{\parallel} \leq \frac{\pi}{a}$. The slope of the dispersion relation becomes zero at the edge of the irreducible Brillouin zone $k_{\parallel} = \frac{\pi}{a}$. This flattening of the dispersion relation creates bandgaps in the photonic crystal band structure. This means that the photonic crystal behaves as a mirror to the bandgap frequencies. Thus, these bandgaps are instrumental in engineering the flow of light.

Photonic band gaps can be used to confine light in standing-wave cavities with long storage times. A defect in the middle of a photonic crystal can confine light of frequencies within the photonic band gap. A larger photonic crystal surrounding the defect allows the resonance in the defect to have a longer lifetime, but it increases the difficulty of coupling light into and out of the cavity. Hence, there is a tradeoff between more photonic crystal unit cells for a higher intracavity lifetime and fewer photonic crystal unit cells for better cavity-to-waveguide coupling. Note that photonic crystal cavities can also be considered an extension of microwave cavities to higher electromagnetic frequencies.

Photonic crystal cavities are useful for enhancing nonlinear optical effects due to their relatively high quality factors (long lifetimes) and relatively small mode volumes. This can lower the power budget for devices requiring second harmonic generation [14]. In particular, photonic crystal cavities that are periodic in one dimension tend to support larger photonic band gaps and tend to maintain their band gaps with lower index contrasts as compared to 2D-periodic photonic crystal cavities [17]. The idea therefore is to engineer the dispersion relation and number of unit cells of the 1D photonic crystal to achieve bandgaps separated by an octave with highly overlapping mode profiles and efficient coupling to the waveguide.

## 1.4 Design Objectives

There are three overarching design objectives for this work:

- **Goal 1 – Dispersion Engineering:** Design a unit cell such that for a certain polarization and a certain frequency range inside a bandgap, the double of that frequency range is also inside another bandgap of the same polarization that is still under the light cone. This is explored in Chapter 2.

- **Goal 2 – Nonlinear Coupling Engineering:** Construct a cavity based on this unit cell and a DC electric field biasing profile to achieve a large nonlinear coupling between the fundamental and second harmonic modes. This sets the stage for achieving large figures of merit $\text{FOM}_1$ and $\text{FOM}_2$. This is the focus of Chapter 3.

- **Goal 3 – Lifetime Engineering:** Optimize the microcavity length such that the dimensionless efficiency per power, $\text{FOM}_1$, is maximized. This corresponds to achieving $Q_1/Q_1^{rad} = Q_2/Q_2^{rad} = 0.5$. This is studied in Chapter 4.

Chapter 5 discusses possibilities for fabrication, design limitations, and avenues for future work.

THIS PAGE INTENTIONALLY LEFT BLANK

# Chapter 2

# Geometric Setup & Unit Cell Design for Octave-Separated Bandgaps

## 2.1 Photonic Crystal Unit Cell Geometry

To satisfy Goal 1 – Dispersion Engineering from Chapter 1, the unit cell must be engineered such that its dispersion relation supports two octave-separated bandgaps. A rendering of the device conceptualized in this treatise is illustrated in Fig. 2-1. Each unit cell is made of silicon and is surrounded by air in all directions. The propagation axis is along the $x-$axis, the height of waveguide structure is along $z-$axis, and the width of structure is along $y-$axis.

The 1D photonic crystal can be viewed as a silicon waveguide Bragg grating with sinusoidal walls and periodic elliptical air holes. Waveguide Bragg gratings with sinusoidally corrugated walls can be fabricated more accurately than waveguide Bragg gratings with rectangularly corrugated walls [18]. Additionally, Bragg-grating photonic crystal waveguides have the potential to be used as an experimental platform for optical manipulation and assembly of ultracold molecules [19]. Furthermore, ridge waveguides with longitudinal sinusoidal width perturbations have been used for second harmonic generation [20].

A summary of the relevant geometric photonic crystal parameters are detailed in Table 2.1. All parameters related to the electrodes will be introduced in the next

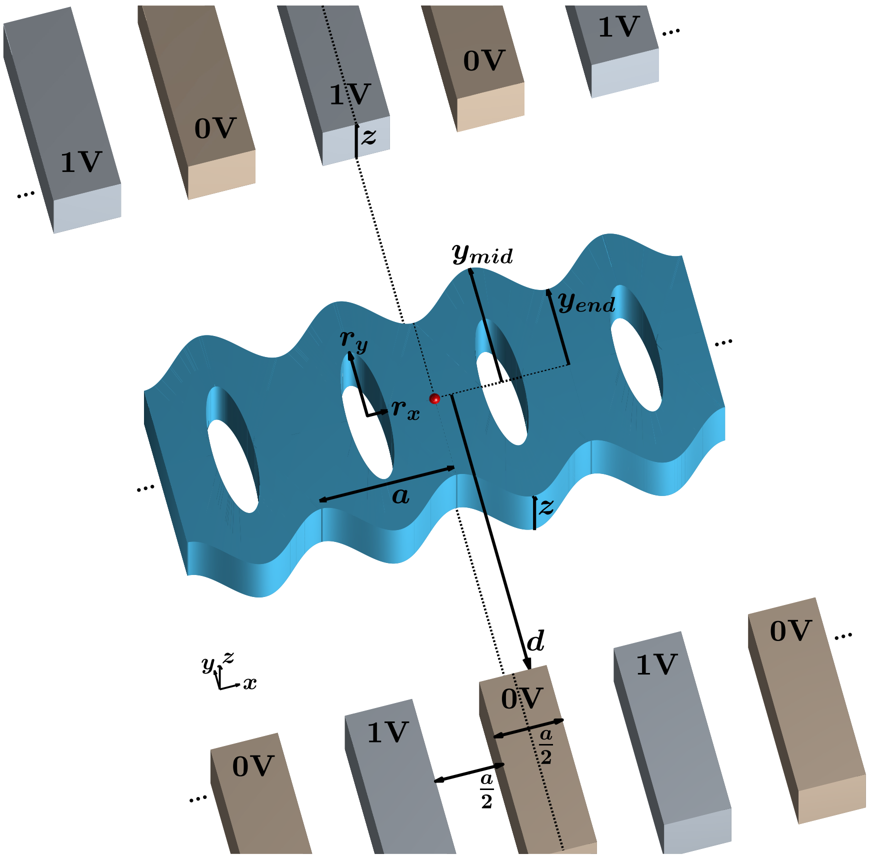

Figure 2-1: 3D rendering of the silicon 1D photonic crystal device concept.

chapter. These are the distances $d$ from the central $xz-$plane of the cavity to the edge of the electrodes, the distances $\frac{a}{2}$ between adjacent electrodes, the +1V and 0V alternating electrode biasing, and the widths, heights, and positions of the electrodes.

## 2.2 MPB Simulation Setup

MPB, which stands for MIT photonic bands, is a free and open-source Python simulation software package that computes dispersion relations and electromagnetic mode profiles of photonic crystal unit cells via a frequency-domain eigenmode solver that solves for harmonic modes of Maxwell's equations [21]. MPB simulates unit cells in normalized units. This means that the lattice constant of the unit cell in the propagation direction is defined as 1 normalized unit.

MPB assumes infinite periodicity of the simulation domain in all three directions

| **Parameter** | **Definition** |
|---|---|
| $\boldsymbol{a}$ | Unit cell length or lattice constant. In normalized units it is always 1. |
| $\boldsymbol{r_x}$ | Length of the minor radius of the elliptical hole, denoted by $x$ since this is parallel to the propagation direction. |
| $\boldsymbol{r_y}$ | Length of the major radius of the elliptical hole, denoted by $y$ since this is perpendicular to the propagation direction. |
| $\boldsymbol{y_{mid}}$ | Distance from central $xz-$plane to sinusoidal wall peak, where this peak is directly above the ellipse in the $y-$direction. |
| $\boldsymbol{y_{end}}$ | Distance from central $xz-$plane to sinusoidal wall trough, where this trough is half a unit cell away from $y_{mid}$ and the center of the ellipse. |
| $\boldsymbol{z}$ | Height of the unit cell |

Table 2.1: Geometric parameters of the photonic crystal unit cell and their corresponding definitions.

in accordance with Bloch's theorem. The unit cell introduced in this chapter can be considered as truly infinitely periodic in the $x-$direction, but is finite in the $y-$ and $z-$directions. Therefore, enough space must be left in the $y-$ and $z-$directions of the simulation domain, such that successive unit cells spaced in the $y$ and $z$ directions are virtually uncoupled. In light of these considerations, all MPB simulations performed for this work use simulation domain sizes of $s_x = 1$, $s_y = 8$, and $s_z = 6$.

An MPB resolution of at least 20 is needed to obtain correct qualitative behavior [22]. This thesis uses a resolution $2^5 = 32$ for increased numerical accuracy. The MPB band simulation is computed over the Irreducible Brillouin Zone, or $0 < \frac{k_x a}{2\pi} \leq 0.5$, with 56 $k-$points per band. 8 $TE$-like and 8 $TM$-like bands are simulated.

Silicon is a dispersive material, which means that its refractive index varies with frequency. At room temperature (293 K), for frequencies near the desired first harmonic ($\approx$ 2.65 $\mu$m), the refractive index of silicon is approximately 3.435, and for frequencies near the desired second harmonic ($\approx$ 1.29 $\mu$m), the refractive index of silicon is approximately 3.503 [23]. To save computation time, the MPB simulation in this chapter uses a midpoint refractive index of 3.47.

## 2.3 Final Band Diagram Results

This section presents a set of parameters for this geometry that satisfy goal 1 and the resulting simulated band diagram. Table 2.2 enumerates the numerical design values of the unit cell parameters in both normalized and SI units.

| **Normalized** | | **Physical** | |
|---|---|---|---|
| **Parameter** | **Value** | **Parameter** | **Value** |
| $\boldsymbol{a/a}$ | 1.00 | $\boldsymbol{a}$ | 575.00 nm |
| $\boldsymbol{r_x/a}$ | 0.15 | $\boldsymbol{r_x}$ | 86.25 nm |
| $\boldsymbol{r_y/a}$ | 0.50 | $\boldsymbol{r_y}$ | 287.50 nm |
| $\boldsymbol{y_{mid}/a}$ | 0.90 | $\boldsymbol{y_{mid}}$ | 517.50 nm |
| $\boldsymbol{y_{end}/a}$ | 0.60 | $\boldsymbol{y_{end}}$ | 345.00 nm |
| $\boldsymbol{z/a}$ | 0.70 | $\boldsymbol{z}$ | 402.50 nm |

Table 2.2: Numerical design values for unit cell parameters in normalized and SI units.

Fig. 2-2 depicts the dispersion relation for the structure shown in Fig. 2-1. The solid shaded region in gray above the light line designates the light cone of extended radiation states. As expected, the lowest band is a TE band [15].

Denote the 1st harmonic dielectric band edge frequency ($TE$ band #1) by $f_{1,1}$.
Denote the 1st harmonic air band edge frequency ($TE$ band #2) by $f_{2,1}$.
Denote the 2nd harmonic dielectric band edge frequency ($TE$ band #7) by $f_{1,2}$.
Denote the 2nd harmonic air band edge frequency ($TE$ band #8) by $f_{2,2}$.

Highlighted in yellow, the first harmonic usable gap is $f_{1,1} < f < \frac{f_{2,2}}{2}$, and the frequency of the fundamental mode must lie within this range. Highlighted in green, the usable second harmonic gap is $2f_{1,1} < f < f_{2,2}$, and the frequency of the second harmonic mode must lie within this range. These usable gap ranges are the frequency

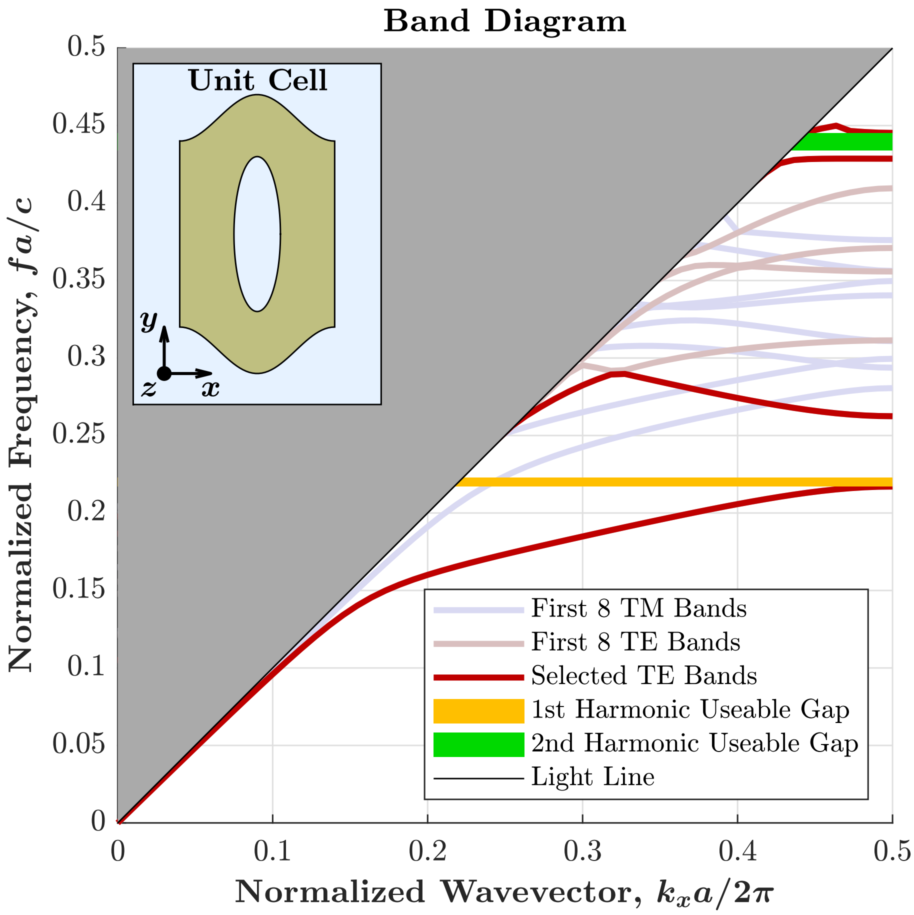

Figure 2-2: 1D photonic crystal band structure result.

ranges in which fundamental and second harmonic resonant modes placed within those regions could simultaneously occur inside the $TE$ band gaps of the photonic crystal unit cell.

Since Eq. (1.5) requires good spatial overlap between the $y-$components of the first and second harmonic cavity modes to have a high dimensionless nonlinear coupling coefficient $\bar{\beta}$, it is therefore important that the $y-$components of the photonic crystal unit cell modes corresponding to the edges of the $TE$ band are also spatially overlapping. This was found to be the case for the unit cell design and parameters discussed in this chapter.

By designing a 1D photonic crystal unit cell with a sinusoidal wall, elliptical holes, and bandgaps containing the first and second harmonic frequencies, the unit cell dispersion relation was successfully engineered. This unit cell is the keystone of the photonic crystal cavities that are synthesized and analyzed in the following chapters.

# Chapter 3

# Photonic Crystal Cavity Design Approach

## 3.1 Recipe for Deterministic Design of Ultra-High $Q$-Factor Microcavities

A 1D array of photonic crystal unit cells can be converted into a cavity by introducing a defect or parameter perturbation at the center of the array. This causes the unit cells on each side of the center to behave as mirrors at the bandgap frequencies, forming a Fabry-Pérot-like cavity. The photonic band structure from Chapter 2 can now be used to deterministically construct a 1D photonic crystal nanobeam cavity with ultra-high quality factor, following the recipe detailed in Ref. [24].

1. The quality factor $Q$ of a Bragg mirror cavity can be maximized with Gaussian-shaped field attenuation inside the cavity's mirrors [25]. Ref. [24] demonstrates that for a cavity with Gaussian confinement, **the optimal defect length is $L = 0$.**

2. To reduce scattering inside the device and to maintain a constant phase velocity at $\pi/a$ [24], the unit cell length $a$ should be fixed for the entirety of the photonic crystal nanobeam cavity. This work uses a **fixed lattice constant**

**$a = 575$ nm.**

3. In order to achieve the desired Gaussian attenuation, **the mirror strength must increase linearly with unit cell distance from the center of the cavity.** This forms a modulated Bragg mirror [24]. Let $\omega_{\text{res}}$ be the cavity resonant frequency. Let $\omega_1$ be the dielectric band edge frequency (lower bandgap frequency), let $\omega_2$ be the air band edge frequency (upper bandgap frequency), and let $\omega_0 = \frac{\omega_1+\omega_2}{2}$ be the midgap frequency, for a certain unit cell inside the cavity. Then, the mirror strength $M$ of this unit cell inside the cavity is defined as

$$M = \sqrt{\frac{(\omega_2 - \omega_1)^2}{(\omega_2 + \omega_1)^2} - \frac{(\omega_{res} - \omega_0)^2}{\omega_0^2}} \tag{3.1}$$

Using the unit cell from Chapter 2 as the central cavity unit cell, this high-$Q$ cavity recipe from Ref. [24] is used as the basis for designing a microcavity to have a high quality factor at both octave-separated frequencies. Note that our unit cell has two sets of lower and upper bandgap frequencies, one set $\omega_{1_1}$, $\omega_{2_1}$ for the first harmonic formed from $TE$ bands 1 and 2, and another set $\omega_{1_2}$, $\omega_{2_2}$ for the second harmonic formed from $TE$ bands 7 and 8. It is therefore non-trivial to co-design the first and second harmonic mirror strength profiles such that both are linear over the same set of unit cells and have similar magnitudes.

## 3.2 Design of Cavity Tapering Profile

Unlike in Chapter 2 where the midpoint refractive index was used in the MPB simulation, here the silicon refractive index of 3.503 is used for the second harmonic bands ($TE$ 7 and $TE$ 8), and the silicon refractive index of 3.435 is used for the fundamental harmonic bands ($TE$ 1 and $TE$ 2). Furthermore, only the $k_x = 0.5$ (normalized units) point, which corresponds to the edge $k_x = \frac{\pi}{a}$ of the irreducible Brillouin zone, is simulated, and only the 1st, 2nd, 7th, and 8th $TE$ bands are saved. In each simulation the minor $r_x$ and major $r_y$ radii of the elliptical air holes are the physical parameters which are adjusted in each unit cell according to the tapering profile under optimization.

Let $p$ be a nonnegative integer denoting unit cell position along the profile, and let $N$ be the total number of unit cells under consideration ($p = 1, 2, \ldots, N$). In this optimization $N = 25$. Let the tapering profile $r_x(p),\ r_y(p)$ denote the chosen physical parameters as a function of unit cell position, let the actual mirror strength profiles $M_{1_{act}}(p)$ and $M_{2_{act}}(p)$ denote the resulting mirror strengths as a function of unit cell position, and let the desired mirror strength profiles $M_{1_{des}}(p)$ and $M_{2_{des}}(p)$ denote linear mirror strengths as a function of unit cell position. This work assumes $M_{1_{des}}(p) = M_{2_{des}}(p) = M_{des}(p)$. $M_{1_{act}}(r_x, r_y),\ M_{2_{act}}(r_x, r_y)$ are the actual functions relating the physical parameters of a unit cell to its mirror strengths.

In general, linear $r_x(p)$ and linear $r_y(p)$ will yield nonlinear $M_{1_{act}}(p)$ and nonlinear $M_{2_{act}}(p)$, and vice-versa. Thus, the goal is to determine a nonlinear $r_x(p),\ r_y(p)$ that will give a linear $M_{1_{act}}(p),\ M_{2_{act}}(p)$. The co-optimization procedure is performed as follows:

- **Step 0:** Start with an initial $r_x(p),\ r_y(p)$ over the ranges that can sustain a second harmonic mode within the bandgap between $TE$ bands 7 and 8.

- **Step 1:** In MPB, for all $p$, simulate the lower and upper bandgap frequencies for the fundamental and second harmonic modes $\omega_{1_1},\ \omega_{2_1},\ \omega_{1_2},\ \omega_{2_2}$.

- **Step 2:** In MATLAB, use $\omega_{1_1}(p),\ \omega_{2_1}(p),\ \omega_{1_2}(p),\ \omega_{2_2}(p)$ from Step 1 to compute $M_{1_{act}}(p),\ M_{2_{act}}(p)$. This gives a sampling of the $M_{1_{act}}(r_x, r_y)$ and $M_{2_{act}}(r_x, r_y)$ functions.

  If the actual profiles $M_{1_{act}}(p),\ M_{2_{act}}(p)$ are sufficiently close to the desired linear profiles $M_{1_{des}}(p),\ M_{2_{des}}(p)$, ***exit the process.*** In this work, the exit condition is the Normalized Root Mean Squared Errors $NRMSE_{1,2} < 0.05$:

$$NRMSE_{1,2} = \frac{\sqrt{\frac{1}{N}\sum_{p=1}^{N}\left[M_{1,2_{act}}(p) - M_{des}(p)\right]^2}}{\sqrt{\frac{1}{N}\sum_{p=1}^{N}\left[M_{des}(p)\right]^2}} \tag{3.2}$$

- **Step 3:**
  - **3a:** Construct the inverse functions $r_x(M_{1_{act}}),\ r_y(M_{1_{act}})$ and interpolate $r_x,\ r_y$ onto the $M-$points corresponding to $M_{1_{des}}(p)$. This returns $r_{x_{new_1}}(p),\ r_{y_{new_1}}(p)$.
  - **3b:** Construct the inverse functions $r_x(M_{2_{act}}),\ r_y(M_{2_{act}})$ and interpolate $r_x,\ r_y$ onto the $M-$points corresponding to $M_{2_{des}}(p)$. This returns $r_{x_{new_2}}(p),\ r_{y_{new_2}}(p)$.
- **Step 4:**
  - **4a:** Interpolate $M_{2_{act}}$ onto $r_{x_{new_1}}(p),\ r_{y_{new_1}}(p)$ from Step 3a and compare the interpolated $M_{2_{act}}^{intp}(p)$ to $M_{2_{des}}(p)$
  - **4b:** Interpolate $M_{1_{act}}$ onto $r_{x_{new_2}}(p),\ r_{y_{new_2}}(p)$ from Step 3b and compare the interpolated $M_{1_{act}}^{intp}(p)$ to $M_{1_{des}}(p)$.
- **Step 5:** If $M_{2_{act}}^{intp}(p)$ is closer to $M_{2_{des}}(p)$ than $M_{1_{act}}^{intp}(p)$ is to $M_{1_{des}}(p)$, select $r_{x_{new}}(p) = r_{x_{new_1}}(p),\ r_{y_{new}}(p) = r_{y_{new_1}}(p)$.

  Else, select $r_{x_{new}}(p) = r_{x_{new_2}}(p),\ r_{y_{new}}(p) = r_{y_{new_2}}(p)$
- **Step 6:** Return to Step 1 with the updated $r_{x_{new}}(p),\ r_{y_{new}}(p)$.

The final tapering profile $r_x(p),\ r_y(p)$ is placed on both halves of the cavity. The results of this optimization procedure are illustrated in Fig. 3-1. The center of the cavity is unit cell number 50 which corresponds to $p = 1$, and unit cell numbers 26 and 74 correspond to $p = N = 25$. Following Ref. [26] an additional section of, in this work 25, maximum mirror strength unit cells is added to both ends of the cavity to obtain a radiation-limited cavity.

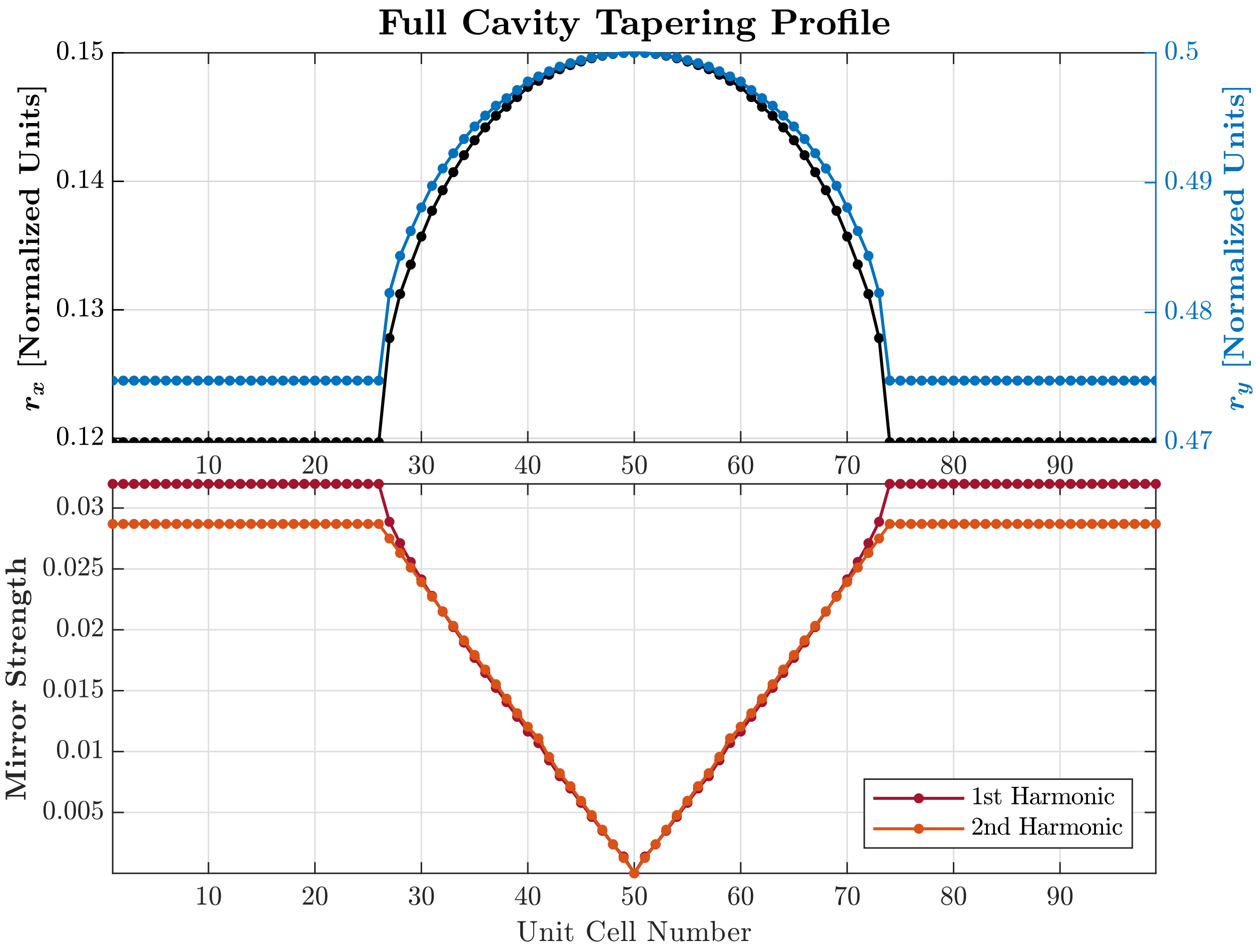

Figure 3-1: (a) *Top:* Final nonlinear $r_x(p),\ r_y(p)$ tapering profile. (b) *Bottom:* Final linear $M_{1_{act}}(p),\ M_{2_{act}}(p)$ mirror strength profiles for the first and second harmonic modes.

As seen in Fig. 3-1(b), the tapering profile was successfully designed such that the mirror strength curves for the first and second harmonics are both approximately linear and equal over the entirety of the tapered region. It is interesting to note that the specific resulting nonlinear shapes of $r_x(p),\ r_y(p)$ are similar in such a way that $r_y(p)$ is related to $r_x(p)$ by a linear rescaling plus offset.

## 3.3 Electrode Geometry

Now that the cavity geometry has been designed, it is time to consider the electrode geometry which is needed for Electric Field-Induced Second Harmonic (EFISH) generation. To reduce losses due to optical absorption, the electrodes will be made out of doped silicon instead of metal.

The distance from the electrodes to the cavity must be carefully selected. On one hand, if the electrodes are placed too far from the cavity, there would be a very weak DC field inside the cavity, resulting in a weak $\chi^{(2)}_{induced}$ and thus weak second-harmonic generation. On the other hand, if the electrodes are placed too close to the cavity, light will couple into the silicon electrodes as if they were waveguides, which deteriorates the lifetimes of photons in the cavity and hence diminishes the system's quality factors and second harmonic generation figures of merit.

Returning to Fig. 2-1 from Chapter 2, $d = 1.25$ $\mu$m is the chosen distance from the central $xz-$plane of the cavity to the edge of the electrodes. The height of the electrodes is the same $z$ as the height of the nanobeam structure. The $x-$distance from the start of one electrode to the start of the next electrode is the same $a$ as the lattice constant of the photonic crystal unit cells. The electrode $x-$width is a half period $\frac{a}{2}$, and the distance to the next electrode is another half period $\frac{a}{2}$. Electrodes on opposite sides of the device are spatially aligned with each other.

The electric field set up by the electrodes is only useful in the silicon-dominated regions of the photonic crystal device (as opposed to the air hole regions), as this is where EFISH can occur. Furthermore, the majorities of the optical modes of the MPB unit cell were found to exist in the silicon-dominated regions of the structure. Hence, the electrodes are centered such that each electrode's central $x-$position is midway between the $x-$positions of the two nearest air holes. This way the highest intra-cavity DC electric field, which induces the highest intra-cavity $\chi^{(2)}_{induced}$, is co-located with the highest intra-cavity optical field. The spatial alternation in the electrode biasing pattern will be discussed later in this chapter.

The cavity and electrode geometry is generated in Python using the `gdspy` package. The GDSII file that describe the $xy-$cross section of the waveguide and electrodes is imported into LUMERICAL and COMSOL, where the $z$ height of the system is then entered.

## 3.4 LUMERICAL FDTD Simulation Setup

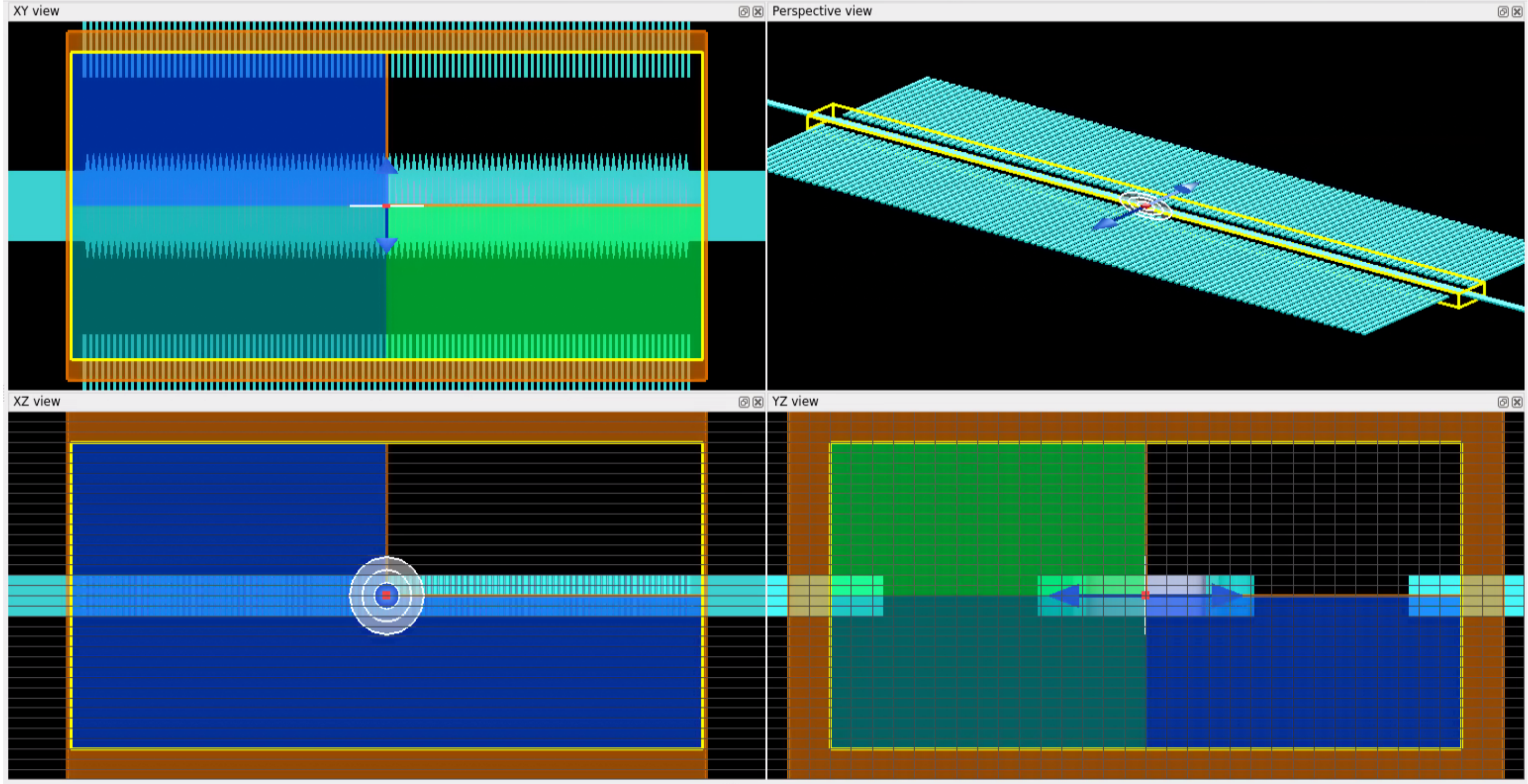

Figure 3-2: LUMERICAL illustration of symmetry conditions and source positioning. The device geometry is not rendered to scale.

LUMERICAL FDTD is a photonic simulation software package that uses the Finite Difference Time-Domain (FDTD) method for solving Maxwell's Equations at optical frequencies. Here LUMERICAL FDTD is used to simulate the electric field profile of the fundamental and second harmonic modes inside the photonic crystal microcavity structure, and to extract the quality factors of these modes.

The FDTD simulations use a simulated time of 60 picoseconds, room temperature (300 K), and a background material of air ($n = 1$). The simulation domain has a

$y-$span of 3 $\mu$m, a $z-$span of 3 $\mu$m, and an $x-$span of 60 $\mu$m. The auto non-uniform mesh is used with a LUMERICAL accuracy level of 3, which is categorized by LUMERICAL as a "good tradeoff between accuracy, space memory requirements, and simulation time." Furthermore, since the simulations in this work have no metals or Perfect Electric Conductors (PECs), the conformal variant 0 mesh refinement means that a conformal mesh is applied to the entire simulation region [27]. The $dt$ stability factor is set at 0.99, and the minimum mesh step size is set at 0.25 nm.

Due to the symmetrical nature of the 1D photonic crystal cavity, LUMERICAL symmetry boundary conditions can be exploited to reduce the required simulation time by reducing the size of the simulation domain. The $x_{max}$, $y_{max}$, and $z_{max}$ boundary conditions are PML (Perfectly Matched Layers). The $x_{min}$, $y_{min}$, and $z_{min}$ boundary conditions are symmetric, antisymmetric, and symmetric, respectively, corresponding to the symmetries of the TE-like modes simulated in MPB. These symmetry conditions cut the size of the simulation domain in one-eighth, which significantly reduces the amount of time and storage required per simulation run.

For all three of the $x_{max}$, $y_{max}$, $z_{max}$ boundary conditions, the stretched coordinate PML type is used. With a standard PML profile on any of the $x_{max}$, $y_{max}$, $z_{max}$ boundary conditions, the simulations diverge, but with a stabilized profile on all three, the simulations successfully converge. However, the increased number of PML layers in the stabilized profile significantly slows down the simulations. Taking the stabilized $\alpha$ of 0.9 [28] instead of the standard $\alpha$ of 0 and keeping all other parameters at the values of the standard profile, the simulation converges and runs in a reasonable time frame.

The simulation source is an electric dipole source placed at the center of the cavity, with an amplitude of 1 and direction angles $\theta = 90°$ and $\phi = 90°$ 3-2. Initial simulations used a relatively broadband pulse to find the approximate frequency range of the cavity resonance. Next, a narrowband input pulse around that frequency is specified so that there are less extraneous frequencies that need to decay, allowing the decay of the cavity resonance to be more clearly ascertained. For the simulation results shown here, for the first harmonic, a standard pulse type optimized for short pulses is utilized with a frequency of 114.605 THz, a pulse length of 1.5 ps, and a pulse center offset of 3 ps. For the second harmonic, a standard pulse type optimized for short pulses is utilized with a frequency of 232.932 THz, a pulse length of 1.5 ps, and a pulse center offset of 3 ps.

Simulating a material without dispersion, or with a fixed refractive index, is much faster than simulating a material with dispersion. Additionally, having two distinct simulation files at the two separate frequencies of interest allows for clearer visualization of power and field decay over time corresponding to each of the fundamental and second harmonic modes. For these reasons, two separate simulations are performed. Each of the two narrow-band simulation files uses a constant refractive index, which approximates the silicon material dispersion around the fundamental or second-harmonic frequencies.

## 3.5 Lumerical FDTD Gridding

Since Lumerical uses the simulation bandwidth in determining the necessary mesh, to maintain grid consistency between the first and second harmonic simulations, the FDTD simulation bandwidth is manually set in both files to be 105 - 240 THz, which corresponds to wavelengths 2.86 $\mu$m - 1.25 $\mu$m, respectively. Moreover, since symmetry has been applied in all three of the $x, y, z$ directions, "force symmetric mesh" is in place for all three axes.

Lumerical also uses refractive index to determine the necessary coarseness of the grid. Therefore, to force the lower frequency simulation to have as fine of a grid as the higher frequency simulation, additional phantom GDS layers with the refractive index of the higher frequency silicon are added underneath the "actual" GDS layers with the lower frequency silicon refractive index. Lumerical takes the higher of these two refractive indices to compute its mesh, thus compelling Lumerical to use consistent meshes for both simulations.

Fig. 3-3(a) shows that the grid computed by Lumerical is uniformly spaced in the $x-$direction and approximately piecewise-uniform in the $y-$ and $z-$directions.

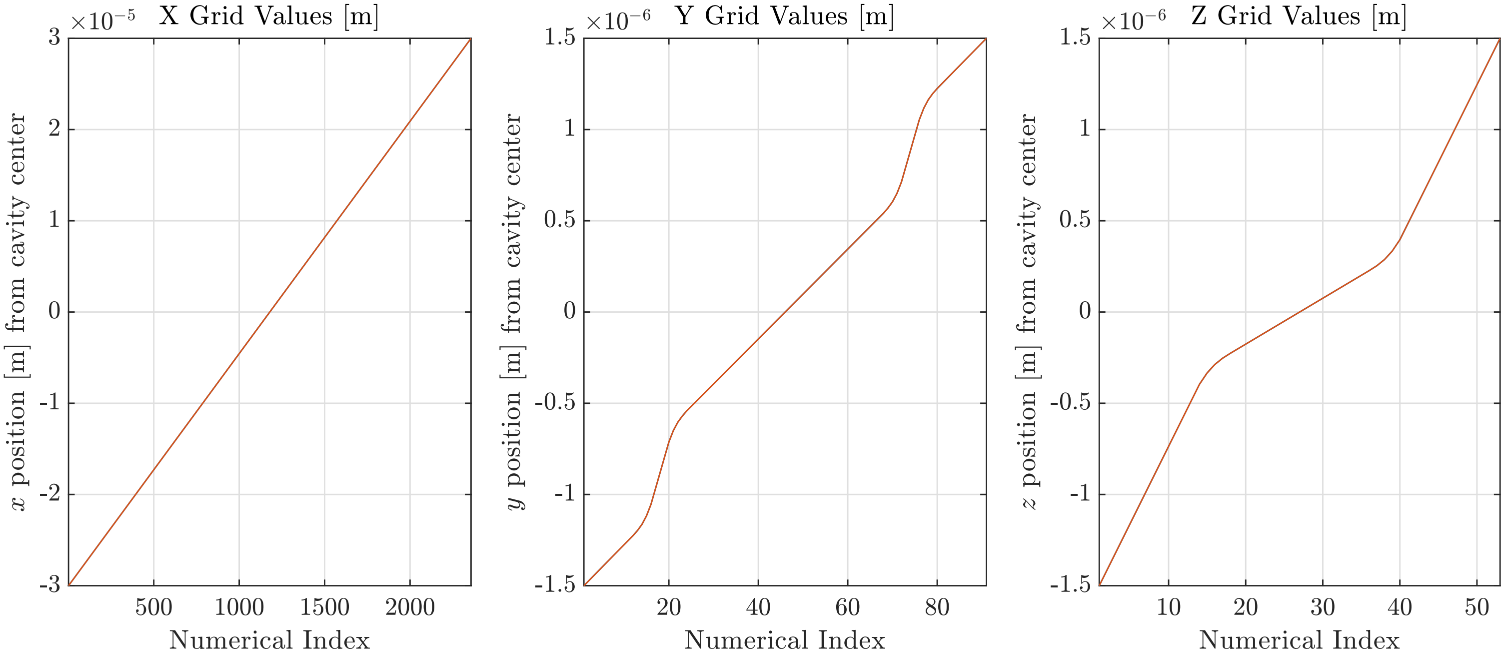

Figure 3-3: (a) *Left:* Uniform LUMERICAL $X-$mesh. (b) *Center:* Nonuniform LUMERICAL $Y-$mesh. (c) *Right:* Nonuniform LUMERICAL $Z-$mesh.

In the $y-$direction, Fig. 3-3(b) depicts a shallower slope (higher resolution) in the central region corresponding to the silicon microcavity and in the two outer regions corresponding to the silicon electrodes on both sides of the cavity. There is a steeper slope (lower resolution) for the air regions on both sides of the cavity before the electrodes. In the $z-$direction, Fig. 3-3(c) shows a steeper slope (lower resolution) for the air regions above and below the device and a shallower slope (higher resolution) for the silicon device region. This specific nonuniform mesh is used for the remainder of this chapter.

## 3.6 Total Quality Factors

Since the fields inside the photonic crystal cavity decay very slowly, the quality factors of the first and second harmonic modes should be determined from the slope of the decaying envelope of the intracavity fields' time evolution [29]. Therefore, the high-$Q$ version of the LUMERICAL Quality Factor Analysis group is used to compute the total quality factor of the resonator.

Geometrically, a square 25 by 25 grid of time monitors is used at the center of the cavity at the upper right section of the central unit cell. The $x$ span is 0.575 $\mu$m, which is the lattice constant and width of the unit cell, and the $y-$span is 0.525 $\mu$m. The center of this grid is the middle of the $x$ span, the middle of the $y$ span, and elevated by $z = 0.1$ $\mu$m above the central $xy-$plane of the structure.

For the first harmonic, the frequency range of analysis is 114 - 115 THz, and for the second harmonic, the frequency range of analysis is 232 - 233 THz. For both modes, the analysis start time is 15 ps, as this is the time after which the transient input source will have fully decayed and dissipated away.

The total quality factors $Q_1$ and $Q_2$ of the fundamental and second harmonic modes are given in Table 3.1.

| | Frequency $f$ (THz) | Wavelength $\lambda$ ($\mu$m) | **Quality Factor $Q_{tot}$** |
|---|---|---|---|
| **1st Harmonic** | 114.6 THz | 2.616 $\mu$m | $\boldsymbol{Q_1 = 1.748 \times 10^5}$ |
| **2nd Harmonic** | 232.9 THz | 1.287 $\mu$m | $\boldsymbol{Q_2 = 4.504 \times 10^4}$ |

Table 3.1: Fundamental and second harmonic resonant frequencies and their corresponding total quality factors $Q_1$ and $Q_2$.

## 3.7 Radiative Quality Factors

In order to calculate the radiative quality factors $Q_1^{rad}$ and $Q_2^{rad}$ one can quantify the power leaving the microcavity, and thus the simulation domain, in different directions using LUMERICAL output power time monitors. Because of symmetry conditions, only one of each $x$, $y$, and $z$ monitor is required, instead of both. Three output power time monitors, an $x-$normal, a $y-$normal, and a $z-$normal, are used, where each monitor fills the entire simulation domain in that planar direction.

Assume that the power $P_x$ crossing the $x-$monitor is essentially coming from waveguide transmission, and negligibly from the air surrounding the silicon structure. Assume that the power emanating through the $y-$ and $z-$monitors, $P_y$ and $P_z$

respectively, is all of the radiated power. Under these assumptions, the transmitted power is $P_x$, and the radiated power is $P_y + P_z$.

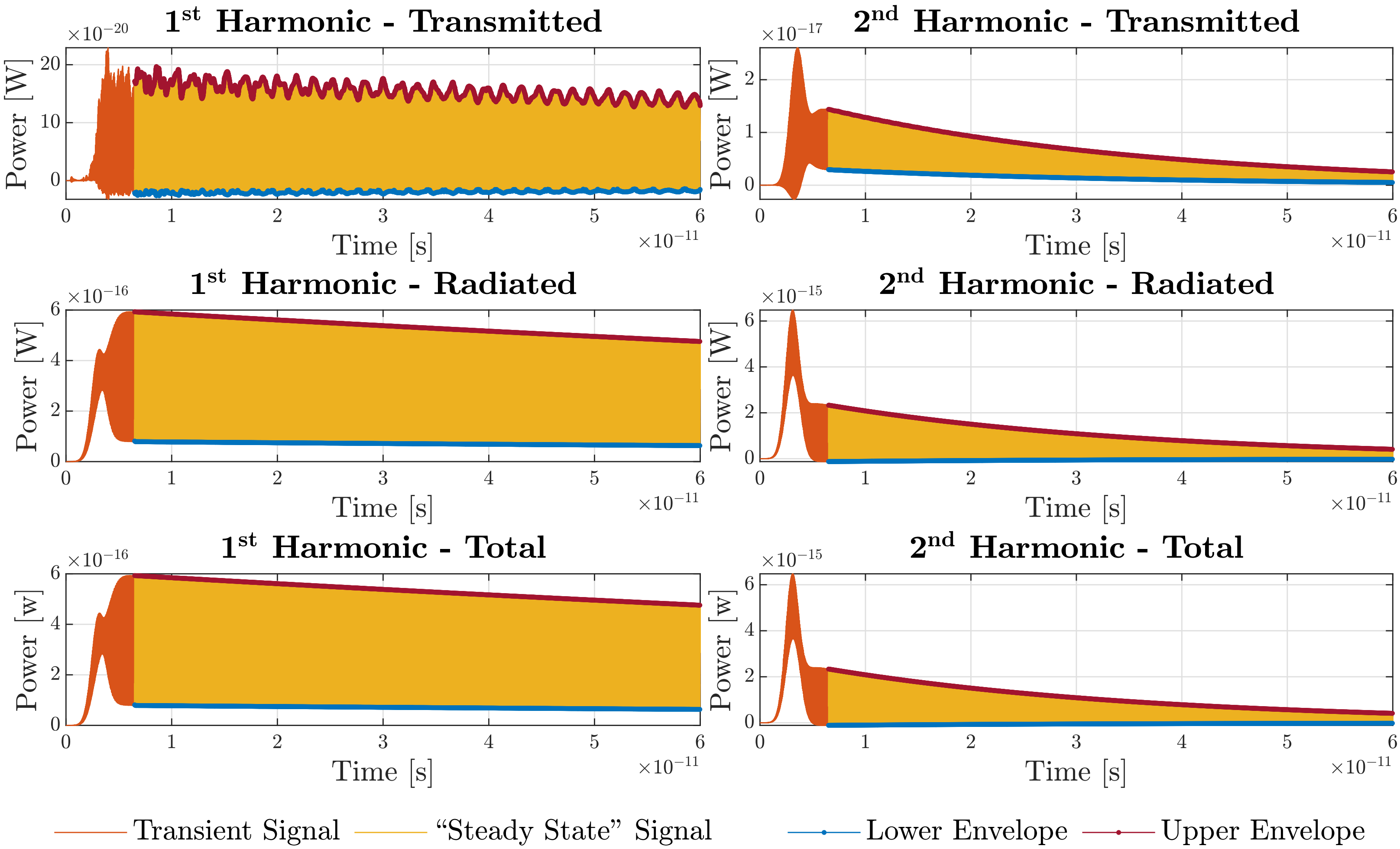

Figure 3-4: *Left Column:* First Harmonic (a-i) Transmitted power, (a-ii) Radiated power, (a-iii) Total power leaving simulation domain. *Right Column:* Second Harmonic (b-i) Transmitted power, (b-ii) Radiated power, (b-iii) Total power leaving simulation domain.

The left and right columns of Fig. 3-4 show the power outputs for the fundamental and second harmonic modes. The 1st, 2nd, and 3rd rows show the transmitted, radiated, and total (transmitted + radiated) powers emanating from the device. The transients in power shown in orange for the first 6.5 ps are due to the presence of the source turning on and then off. After 6.5 ps, it is safe to assume that the cavity has reached its "steady" behavior and only sustains the first and second harmonic modes. All additional extraneous frequencies have already evanescently decayed. This regime is shown in yellow in Fig. 3-4.

The computation procedure for $Q_1^{rad}$ and $Q_2^{rad}$ is as follows:

Let $P_{m_{1,2}}^{tra}(t)$ be the upper envelope of the 1st, 2nd-harmonic transmitted power.

Let $P_{m_{1,2}}^{rad}(t)$ be the upper envelope of the 1st, 2nd-harmonic radiated power.

Let $P_{m_{1,2}}^{tot}(t)$ be the upper envelope of the 1st, 2nd-harmonic total emitted power.

Extract the exponential decay rate $\gamma_{1,2}^{tot}$ from $P_{m_{1,2}}^{tot}(t)$ curve.

$$\begin{aligned} \gamma_{1,2}^{tra} &= \frac{P_{m_{1,2}}^{tra}}{P_{m_{1,2}}^{tot}} \gamma_{1,2}^{tot} & \qquad \gamma_{1,2}^{rad} &= \frac{P_{m_{1,2}}^{rad}}{P_{m_{1,2}}^{tot}} \gamma_{1,2}^{tot} \\ Q_{1,2}^{tra} &= \frac{\omega_{1,2}}{\gamma_{1,2}^{tra}} & \qquad Q_{1,2}^{rad} &= \frac{\omega_{1,2}}{\gamma_{1,2}^{rad}} \end{aligned} \tag{3.3}$$

The transmitted, radiative, and total quality factors for the fundamental and second harmonic modes are given in Table 3.2. As expected from Eq. (1.6), the total quality factor is less than both the transmitted and radiated quality factors. It is interesting to note that since the radiative quality factors are a few orders of magnitude lower than the transmitted quality factors, the total quality factors are very close to the radiative quality factors. This demonstrates that a radiation-limited cavity at both frequencies has been successfully implemented.

| | Waveguide $Q-$Factor | **Scattering $\boldsymbol{Q-}$Factor** | Total $Q-$Factor |
|---|---|---|---|
| **1st Harmonic** | $Q_1^{tra} = 6.035 \times 10^8$ | $\boldsymbol{Q_1^{rad} = 1.749 \times 10^5}$ | $Q_1^{tot} = 1.748 \times 10^5$ |
| **2nd Harmonic** | $Q_2^{tra} = 7.307 \times 10^6$ | $\boldsymbol{Q_2^{rad} = 4.510 \times 10^4}$ | $Q_2^{tot} = 4.504 \times 10^4$ |

Table 3.2: Transmitted, radiated, and total quality factors for the fundamental and second harmonic modes.

## 3.8 Mode Profiles and Overlap

LUMERICAL field monitors, also known as frequency domain power monitors, return quantities such as the output power and the $x, y, z$ components of the electric field, magnetic field, and Poynting vector. For the first harmonic simulation, the 3D field monitor is centered at 114.605 THz, and for the second harmonic simulation, the 3D field monitor is centered at 232.932 THz. The full 3D simulation data is exported. LUMERICAL uses the symmetry rules to unwrap the data from the simulated region to the full domain. To avoid incorporating the source and initial simulation transients, start time apodization is used with an apodization center of 15 ps and an apodization time width of 5 ps.

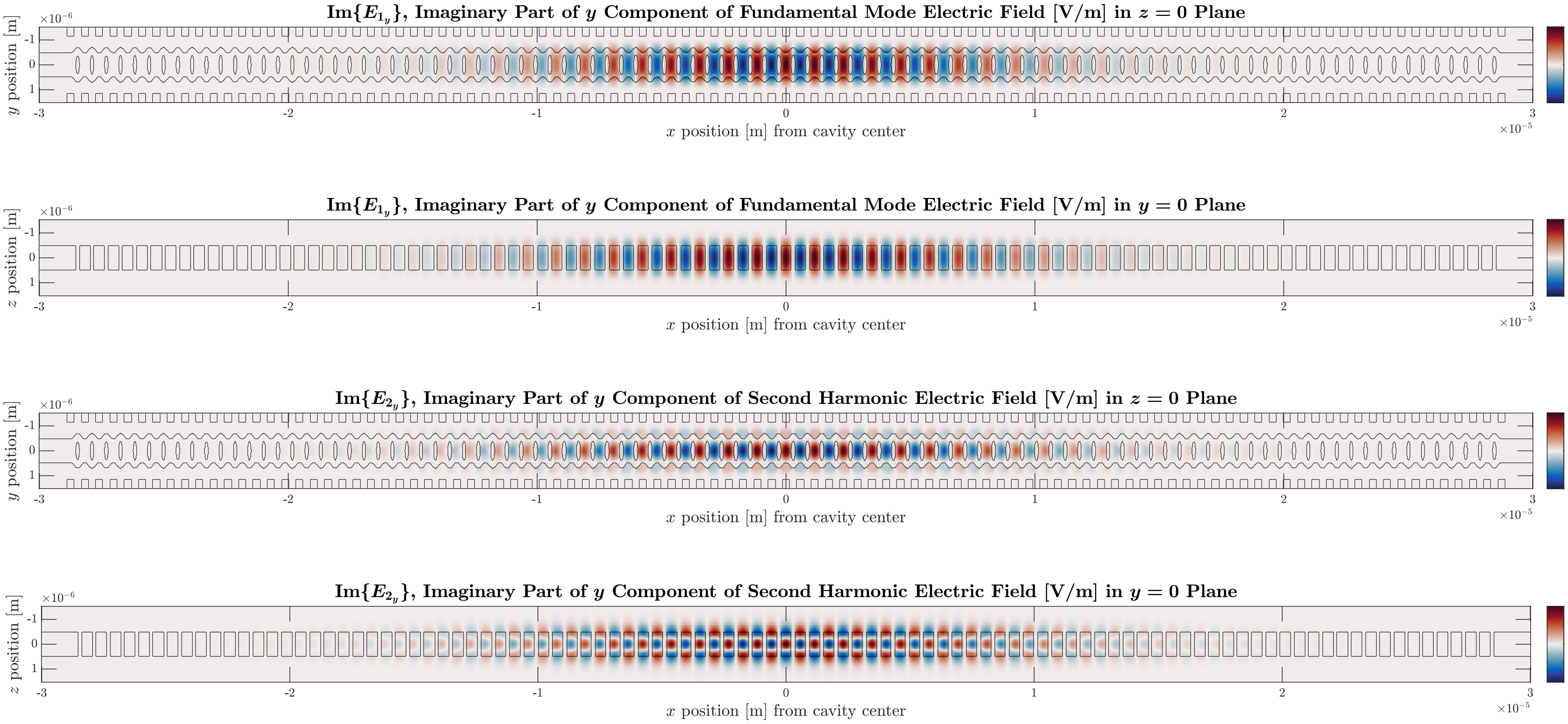

**Im$\{E_{1_y}\}$, Imaginary Part of $y$ Component of Fundamental Mode Electric Field [V/m] in $z = 0$ Plane**

**Im$\{E_{1_y}\}$, Imaginary Part of $y$ Component of Fundamental Mode Electric Field [V/m] in $y = 0$ Plane**

**Im$\{E_{2_y}\}$, Imaginary Part of $y$ Component of Second Harmonic Electric Field [V/m] in $z = 0$ Plane**

**Im$\{E_{2_y}\}$, Imaginary Part of $y$ Component of Second Harmonic Electric Field [V/m] in $y = 0$ Plane**

Figure 3-5: (a) $xy-$cross section of the fundamental mode. (b) $xz-$cross section of the fundamental mode. (c) $xy-$cross section of the second harmonic mode. (d) $xz-$cross section of the second harmonic mode.

Fig. 3-5 shows two cross sections of the imaginary part of the $y-$component of the electric field for the first and second harmonic modes. The sign of the intracavity field alternates with each successive unit cell. This fact is consistent with Bloch's Theorem. Since operation occurs at the edge of the irreducible Brillouin zone $k_x = \frac{\pi}{a}$, the mode solutions are proportional to $e^{ik_x x} = e^{i\frac{\pi}{a}x}$. Thus, the imaginary part of the $y-$component of the electric field is proportional to $\mathrm{Im}\left\{e^{i\frac{\pi}{a}x}\right\} = \sin\left(\frac{\pi}{a}x\right)$, which is periodic with spatial period $\frac{2\pi}{\pi/a} = 2a$. Hence the mode solutions return to the same sign after two unit cells.

According to Eq. (1.5) for the dimensionless coupling coefficient $\bar{\beta}$, the integrand of the numerator depends significantly on the electric field overlap $E_{1_y}^2 E_{2_y}^*$. Fig. 3-6 plots this quantity for two different cross sections and demonstrates that this quantity still alternates its sign every other period. Since $\bar{\beta}$ requires integrating this over the entire cavity, for a material whose $\bar{\varepsilon}(\vec{\boldsymbol{r}})$ does not change sign, $\bar{\beta}$ would be nearly vanishing.

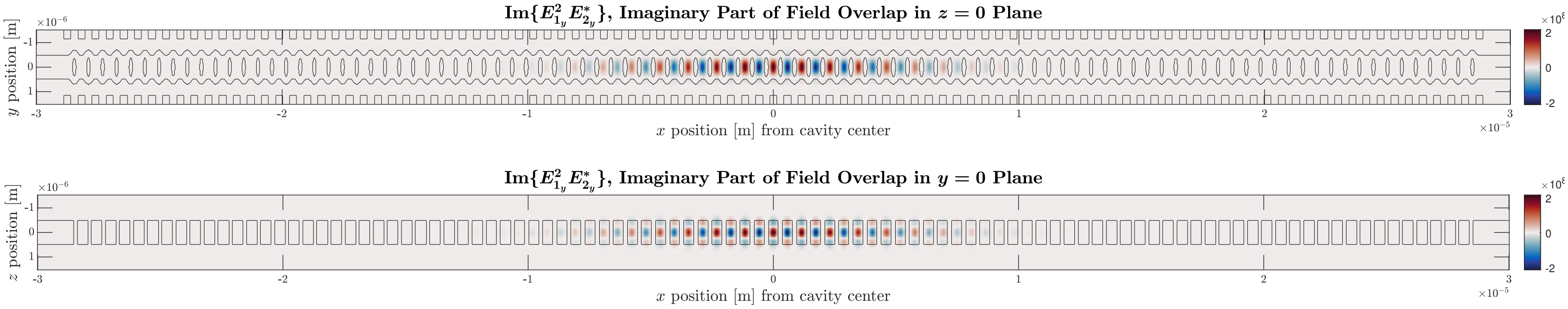

Figure 3-6: (a) *Top:* $xy-$cross section, and (b) *Bottom:* $xz-$cross section, of the optical field overlap used as a factor of the integrand in the numerator of $\bar{\beta}$.

This suggests that it would be advantageous to take the absolute value of this field overlap quantity. If only the $\chi^{(2)}$ could alternate direction and correspondingly change sign with each successive unit cell, this would allow all periods to contribute and not subtract from the integral. Because silicon does not have an intrinsic $\chi^{(2)}$, but can have a $\chi^{(2)}_{induced}$ in the direction of the applied DC electric field, the direction of the second-order nonlinearity can be adjusted by controlling the direction of the applied DC electric fields.

This motivates a spatially alternating DC electric field pattern where the electric field direction in every other period is in opposite directions. Thus, unlike in Ref. [9] where all electrodes on one side of the cavity are biased at the same voltage relative to the other side, implementing this spatially alternating field pattern requires a spatially alternating voltage biasing pattern, where each successive electrode alternates between the bias voltage and ground. This work uses a silicon electrode bias voltage of +1 V.

## 3.9 COMSOL FEM Simulation

The COMSOL Electrostatics Interface is an electrostatics simulation software package that uses the finite element method (FEM) for solving Maxwell's Equations under DC electrostatic conditions. Here, COMSOL is used to simulate the DC electric field profile caused by the spatially-alternating biased electrodes. A DC relative permittivity $\varepsilon_r = 11.7$ is used for silicon. The results of the COMSOL simulation are exported on the same non-uniform LUMERICAL grid shown in Fig. 3-3.

Fig. 3-7 displays the $y-$component of the DC electrostatic field inside the device. A saturated color scale is used to more clearly display the fields inside the cavity as opposed to edge effects near the waveguide. As expected, the field inside the silicon is much lower than the field in air, since silicon behaves as a dielectric material at DC. For this reason, the field is shown only inside the silicon device for clarity. Gray coloring indicates air regions with field not shown.

By centering the doped silicon electrodes on the silicon-dominated region of the unit cell, as opposed to the elliptical air-hole region of the unit cell, an approximately constant electric field predominantly in the $y-$direction is successfully set up in each unit cell. The central upper-electrode is biased at +1 V, and the central lower-electrode is grounded to 0 V. This initiates the spatially alternating pattern, where each successive electrode to the right or left reverses the biasing. This causes the direction of the electric field to be reversed in successive unit cells.

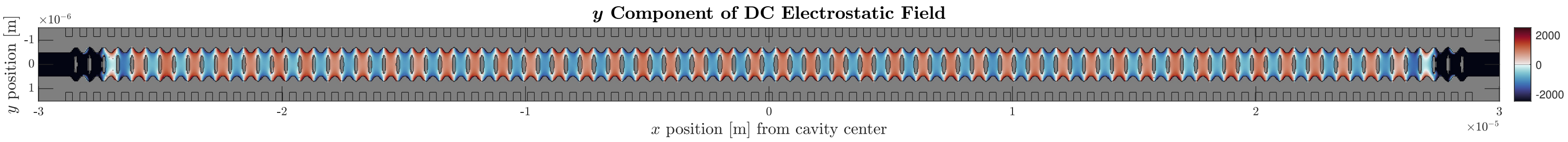

Figure 3-7: Spatially alternating DC field [V/m].

## 3.10 Extension of Second Harmonic Generation Formalism

From Chapter 1, Eq. (1.5) for the dimensionless nonlinear coupling $\bar{\beta}$ was constructed in Ref. [14] by assuming a $\chi^{(2)}$ nonlinearity that does not vary spatially and is constant across the entirety of the structure of interest. However, as seen in Fig. 3-7, the DC electric field $E_{dc,y}(\vec{\boldsymbol{r}})$ changes sign each period, causing $\chi^{(2)}_{\text{induced}}(\vec{\boldsymbol{r}}) = 3\chi^{(3)}E_{dc,y}(\vec{\boldsymbol{r}})$ to alternate sign each period. Also, within each period, there is still a slight spatial variation in $E_{dc,y}(\vec{\boldsymbol{r}})$ and therefore $\chi^{(2)}_{\text{induced}}(\vec{\boldsymbol{r}})$.

Hence, the definition of the dimensionless nonlinear coupling $\bar{\beta}$ from Chapter 1 must be extended to encompass the scenario of a second-order nonlinearity whose sign and value vary spatially:

$$\bar{\beta} = \frac{1}{\overline{\chi}^{(2)}_{\text{effective}}} \frac{\displaystyle\int \chi^{(2)}_{\text{induced}}(\vec{\boldsymbol{r}}) E_{1_y}^2 E_{2_y}^* \; d^3\vec{\boldsymbol{r}}}{\left(\displaystyle\int \varepsilon_1 \left|\vec{\boldsymbol{E}}_1\right|^2 \; d^3\vec{\boldsymbol{r}}\right) \sqrt{\displaystyle\int \varepsilon_2 \left|\vec{\boldsymbol{E}}_2\right|^2 \; d^3\vec{\boldsymbol{r}}}} \sqrt{\lambda_1^3} \tag{3.4}$$

where the original $\bar{\varepsilon}(\vec{\boldsymbol{r}})$ in the numerator integrand is replaced with the actual $\chi^{(2)}_{induced}$ nonlinearity. The expression is then divided by some volumetric average $\overline{\chi}^{(2)}_{\text{effective}}$ in order to maintain normalized units. This mathematical construct is helpful for comparing to the $\bar{\beta}$'s of previous designs in the literature. In this work, the effective second-order nonlinearity $\overline{\chi}^{(2)}_{\text{effective}}$ is defined as

$$\overline{\chi}^{(2)}_{\text{effective}} = \frac{1}{V(W)} \int\limits_{W} \left|\chi^{(2)}_{\text{induced}}\left(\vec{\boldsymbol{r}}\right)\right| \; d^3\vec{\boldsymbol{r}} \tag{3.5}$$

where $W$ denotes the volumetric region of the silicon photonic crystal waveguide over specified lower and upper $x-$bounds, and $V(W)$ is the volume of $W$.

In order to more clearly distinguish the impact of bias voltage level on device performance, it is useful to express $E_{dc,y}\left(\vec{\boldsymbol{r}}\right)$ as the product of a unitless spatial pattern oscillating between $-1$ and 1, $\xi_{dc}\left(\vec{\boldsymbol{r}}\right)$, that is independent of bias voltage and a constant, $E_{dc,y}^{max}$, that is proportional to the bias voltage magnitude.

$$E_{dc,y}\left(\vec{\boldsymbol{r}}\right) = E_{dc,y}^{max}\xi_{dc}\left(\vec{\boldsymbol{r}}\right) \tag{3.6}$$

Therefore,

$$\begin{aligned}
\overline{\chi}_{\text{effective}}^{(2)} &= \frac{1}{V(W)} \int\limits_{W} \left|3\chi^{(3)} E_{dc,y}\left(\vec{\boldsymbol{r}}\right)\right| \, d^3\vec{\boldsymbol{r}} \\
&= \frac{1}{V(W)} \int\limits_{W} \left|3\chi^{(3)} E_{dc,y}^{max}\xi_{dc}\left(\vec{\boldsymbol{r}}\right)\right| \, d^3\vec{\boldsymbol{r}} \\
&= \frac{3\chi^{(3)} E_{dc,y}^{max}}{V(W)} \int\limits_{W} \left|\xi_{dc}\left(\vec{\boldsymbol{r}}\right)\right| \, d^3\vec{\boldsymbol{r}} \qquad (3.7)
\end{aligned}$$

Substituting into $\bar{\beta}$,

$$\begin{aligned}
\bar{\beta} &= \frac{1}{\frac{\cancel{3\chi^{(3)} E_{dc,y}^{max}}}{V(W)} \int_W \left|\xi_{dc}\left(\vec{\boldsymbol{r}}\right)\right| \, d^3\vec{\boldsymbol{r}}} \frac{\int \cancel{3\chi^{(3)} E_{dc,y}^{max}} \xi_{dc}\left(\vec{\boldsymbol{r}}\right) E_{1_y}^2 E_{2_y}^* \, d^3\vec{\boldsymbol{r}}}{\left(\int \varepsilon_1 \left|\vec{\boldsymbol{E}}_1\right|^2 \, d^3\vec{\boldsymbol{r}}\right) \sqrt{\int \varepsilon_2 \left|\vec{\boldsymbol{E}}_2\right|^2 \, d^3\vec{\boldsymbol{r}}}} \sqrt{\lambda_1^3} \\
&= \frac{V(W)}{\int_W \left|\xi_{dc}\left(\vec{\boldsymbol{r}}\right)\right| \, d^3\vec{\boldsymbol{r}}} \frac{\int \xi_{dc}\left(\vec{\boldsymbol{r}}\right) E_{1_y}^2 E_{2_y}^* \, d^3\vec{\boldsymbol{r}}}{\left(\int \varepsilon_1 \left|\vec{\boldsymbol{E}}_1\right|^2 \, d^3\vec{\boldsymbol{r}}\right) \sqrt{\int \varepsilon_2 \left|\vec{\boldsymbol{E}}_2\right|^2 \, d^3\vec{\boldsymbol{r}}}} \sqrt{\lambda_1^3} \qquad (3.8)
\end{aligned}$$

Since only the position of the second-order nonlinearity, and not its physical value, appears in Eq. (3.8), $\bar{\beta}$ can be used to compare designs implemented in different material platforms.

## 3.11 Effective Second-Order Nonlinearity

It can be seen from Fig. 3-7 that the DC field repeats every two unit cells, except near the far left and right ends of the cavity where edge effects dominate. Near the device-waveguide interface, the far left and far right electrode pairs do not have another adjacent electrode pair of opposite polarity to reduce the total field at that location. This causes the electric field in the waveguide right outside the cavity and electrodes to have a much larger magnitude than inside the cavity. Before these edge effects are reached, the volumetric average calculated in Eq. (3.5) should be the same when computed over any range of unit cells symmetric around the center of the cavity. In practice, due to the finite resolution of the structure simulated in COMSOL, there will be slight numerical differences between volumetric averages integrated over different $x-$ranges.

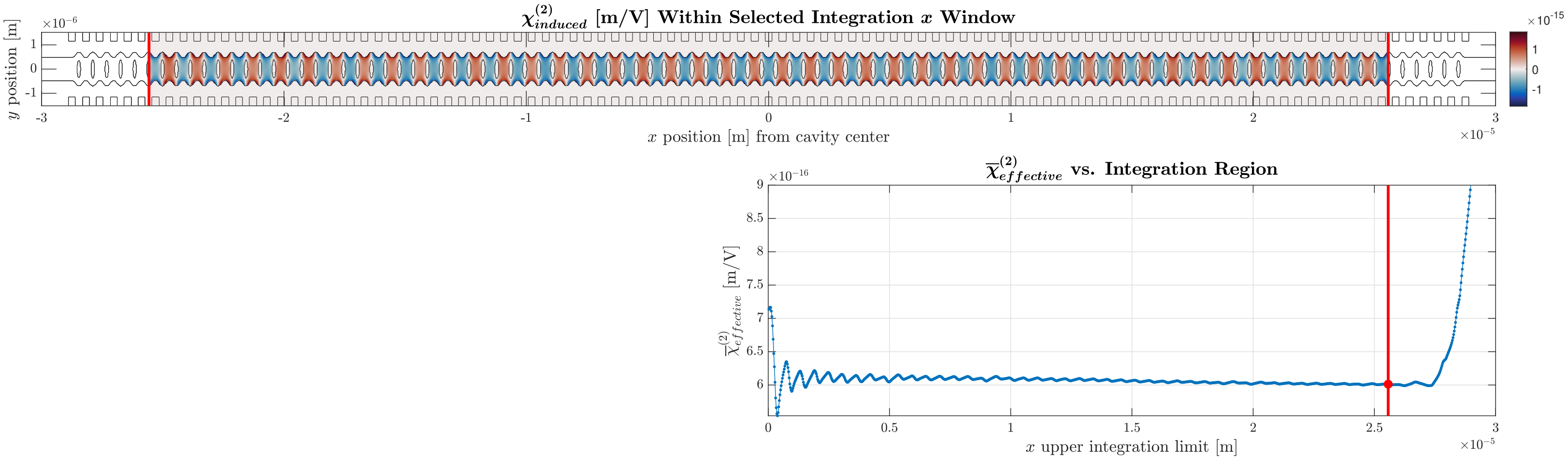

Figure 3-8: (a) *Top:* $\chi^{(2)}_{induced}$ over the selected $x-$integration region. (b) *Bottom:* Variation in the volumetric average $\overline{\chi}^{(2)}_{\text{effective}}$ as a function of symmetric $x-$integration range.

Fig. 3-8(b) displays the numerical variation of $\overline{\chi}^{(2)}_{\text{effective}}$ as the $x-$integration range, which is symmetric about the center of the cavity, increases. As expected, for very small $x-$integration ranges, each additional pixel corresponds to a larger contribution to the integral, causing relatively large numerical oscillations. A spatially accurate value is reached for $x-$ranges larger than $\approx [-20,\ 20]\ \mu$m.

For $x-$ranges beyond the red line in Fig. 3-8(a) and (b), edge effects become non-negligible. As the electric field saturates, the $\chi^{(2)}_{induced}$ saturates, and the $\overline{\chi}^{(2)}_{\text{effective}}$ grows linearly. Thus the red line which corresponds to an integration $x-$range $[-25.57,\ 25.57]\ \mu$m is selected. For this integration region,

$$\overline{\chi}^{(2)}_{\text{effective}} = 6.012 \times 10^{-16}\ \text{m/V}$$

As $\overline{\chi}^{(2)}_{\text{effective}}$ is a constant inherent to the device at a DC electrode bias of 1 V, this value will be used throughout.

## 3.12 Resulting Figures of Merit

Using this modified expression for $\bar{\beta}$, the figures of merit are listed in Table 3.3.

| **Structure** | $\lvert\bar{\boldsymbol{\beta}}\rvert$ | $\mathbf{FOM_1}$ | $\mathbf{FOM_2}$ |
|---:|:---:|:---:|:---:|
| ***This work:* Si PhC Nanobeam** | **0.0085** | **10.8** | $\mathbf{1.003 \times 10^{11}}$ |
| GaAs PhC Nanobeam [17] | 0.00021 | 820 | $1.8 \times 10^8$ |
| AlGaAs/$Al_2O_3$ micropost [14] | 0.018 | $7.5 \times 10^6$ | $8.3 \times 10^{11}$ |

Table 3.3: Comparison of achieved Figures of Merit (FOMs) with preexisting designs in the literature. Note that the micropost design and this work's silicon microcavity design are only simulated whereas the GaAs microcavity design is also experimentally verified.

Although the $\bar{\beta}$ and $FOM_2$ values for this silicon photonic crystal device are competitive with the literature [14, 17], $FOM_1$ is significantly lower. A high intrinsic $FOM_2$ means that this cavity could be effective for second harmonic generation. However, the lower $FOM_1$ indicates that light can't effectively couple into and out of the cavity. This can be seen from the fact that $Q$ and $Q^{rad}$ are almost equal, which means this device operates far into the under-coupled regime.

This suggests that reducing the length of the cavity by reducing the number of unit cells on each side of the cavity center, which would reduce the total quality factor, could be useful to increase $FOM_1$. This is explored in the next chapter of the exposition.

# Chapter 4

# Cavity Length Optimization

## 4.1 Simulation Approach for Enhancing SHG Efficiency Per Power

The end of Chapter 3 concluded that it would be advantageous to explore reducing the number of unit cells for increasing the second harmonic generation unitless efficiency per power $\mathrm{FOM}_1$. In order to do this, this work uses a spatial windowing technique to reduce the design time required for investigating many cavity sizes. Note that based on Fig. 3-8, as long as the cavity contains more than a total of 20 unit cells, $\overline{\chi}^{(2)}_{\text{effective}}$ remains approximately the same regardless of the size of the cavity. Therefore, COMSOL DC electric field simulations do not need to be repeated, and only LUMERICAL photonic simulations need to be carried out.

For this cavity design and LUMERICAL simulation setup, the majority of the light is confined towards the center of the simulation region, and the PML layers function sufficiently well such that they prevent back reflections of the exiting field into the simulation domain. Therefore, moving the PML layers inwards along the $x-$axis should effectively reduce the number of unit cells in the cavity. This can work since the entire taper profile from Chapter 3 is not being compressed into a smaller number of unit cells but rather is simply being truncated by the PML layers at a smaller unit cell number from the center of the cavity. Essentially, smaller cavities are being simulated by simply shrinking the $x-$extent of the simulation domain on the larger geometry file.

The PML is shifted inward by integer multiples of the lattice constant and is placed at the position along the unit cell where the unit cell's width is $y_{end}$ and hence equal to the waveguide width. This means that duplicating the pixel layer right before the PML through the PML would look like the former waveguide segment. For the structure in Chapter 3, moving the PML layers inwards such that the waveguide segments at the ends of the geometry were no longer part of the simulation domain negligibly impacted the fields and figures of merit. Thus, this method of reducing the simulation domain is applied for exploring cavities containing different numbers of unit cells. All LUMERICAL settings from the previous chapter were applied to all of the cavities in this chapter. Furthermore, each cavity length continues to correspond to 2 separate LUMERICAL simulations, one at the first harmonic frequency and one at the second harmonic frequency.

## 4.2 Results of Sweep on Unit Cell Count

Following the approach outlined in the previous section, 12 unique total cavity sizes were tested: $\{30, 40, 50, 54, 56, 58, 60, 66, 70, 80, 90, 100\}$. This corresponds to $\{15, 20, 25, 27, 28, 29, 30, 33, 35, 40, 45, 50\}$ unit cells on each half of the cavity, respectively.

Fig. 4-1(a) shows the variation in the radiative quality factors and total quality factors for different total numbers of unit cells in the cavity. Fig. 4-1(b) displays the ratios $\frac{Q_1^{tot}}{Q_1^{rad}}$ and $\frac{Q_2^{tot}}{Q_2^{rad}}$, which vary roughly sigmoidally with the size of the cavity. For total numbers of unit cells larger than 70, $Q_1^{tot} \approx Q_1^{rad}$ and $Q_2^{tpt} \approx Q_2^{rad}$. This corresponds to the under-coupled device operation. For 56 total unit cells in the cavity, $Q_1^{tot} \approx \frac{Q_1^{rad}}{2}$ and $Q_2^{tot} \approx \frac{Q_2^{rad}}{2}$, making this cavity critically coupled. For fewer total numbers of unit cells the cavity becomes over-coupled. In this region, the total quality factors $Q_1^{tot}$ and $Q_2^{tot}$ grow exponentially as the number of unit cells in the cavity is increased.

Fig. 4-2(a) shows $\text{FOM}_2$ on a zoomed in scale and Fig. 4-2(b) plots $\text{FOM}_1$, which is always less than $\text{FOM}_2$. This is the case because $\text{FOM}_2$ is an intrinsic upper bound on the performance of the cavity and $\text{FOM}_1$ represents an achievable unitless efficiency per power. As the total number of unit cells in the cavity is changed, $\text{FOM}_2$ varies within 1 order of magnitude, whereas $\text{FOM}_1$ varies within 10 orders of magnitude. $\text{FOM}_1$ has a theoretical maximum of $\text{FOM}_{1max} = \dfrac{\text{FOM}_2}{64}$ [14]. It is evident that the maximum $\text{FOM}_1$ occurs for a total cavity size of 56 unit cells, which is depicted by the yellow line in Figs. 4-1 and 4-2. As expected, $\text{FOM}_1$ is maximized when the cavity is critically coupled. For 56 unit cells, $\text{FOM}_1 = \dfrac{\text{FOM}_2}{64.87}$, which is very close to the theoretical $\text{FOM}_{1max}$.

It can be seen in Fig. 4-2(b) that for over 70 total unit cells $\text{FOM}_1$ rapidly deteriorates, and by a 100 total unit cells, the cavity simulated in Chapter 3, $\text{FOM}_1$ has essentially vanished. It is interesting to note that this deterioration is occurring within the last 25 unit cells on each side of the cavity, which are the repeated fixed mirror strength unit cells seen in Fig. 3-1 from Chapter 3. The optimal cavity size of 56 unit cells corresponds to only 3 fixed mirror strength unit cells on each side of the cavity. These observations indicate that the fixed mirror strength additions to the ends of the cavity were essentially unnecessary.

## 4.3 Figures of Merit Summary

The transmitted, radiative, and total quality factors for the fundamental and second harmonic modes of the optimized photonic crystal nanobeam structure are given in Table 4.1. As expected from Eq. (1.6), the total quality factor is less than both the transmitted and radiated quality factors. Since the transmitted quality factors are now of the same order of magnitude as the radiative quality factors, the total quality factors are now reduced. $\frac{Q_1^{tot}}{Q_1^{rad}} = 0.533$ and $\frac{Q_2^{tot}}{Q_2^{rad}} = 0.466$ demonstrate that a critically coupled cavity at both frequencies has been successfully implemented.

The figures of merit of the optimized silicon photonic microcavity are listed in Table 4.2.

|  | Waveguide $Q-$Factor | **Scattering $\boldsymbol{Q}-$Factor** | Total $Q-$Factor |
|---|---|---|---|
| **1st Harmonic** | $Q_1^{tra} = 2.285 \times 10^5$ | $\boldsymbol{Q_1^{rad} = 2.043 \times 10^5}$ | $Q_1^{tot} = 1.090 \times 10^5$ |
| **2nd Harmonic** | $Q_2^{tra} = 1.877 \times 10^4$ | $\boldsymbol{Q_2^{rad} = 2.760 \times 10^4}$ | $Q_2^{tot} = 1.287 \times 10^4$ |

Table 4.1: Updated transmitted, radiated, and total quality factors for the fundamental and second harmonic modes.

| **Structure** | $\boldsymbol{\lvert\bar{\beta}\rvert}$ | $\mathbf{FOM_1}$ | $\mathbf{FOM_2}$ |
|---|---|---|---|
| ***This work:* Si PhC Nanobeam** | **0.00867** | $\boldsymbol{1.334 \times 10^9}$ | $\boldsymbol{8.657 \times 10^{10}}$ |
| GaAs PhC Nanobeam [17] | 0.00021 | 820 | $1.8 \times 10^8$ |
| AlGaAs/$Al_2O_3$ micropost [14] | 0.018 | $7.5 \times 10^6$ | $8.3 \times 10^{11}$ |

Table 4.2: Comparison of optimized Figures of Merit (FOMs) with preexisting designs in the literature. Note that the micropost design and this work's silicon microcavity design are only simulated whereas the GaAs microcavity design is also experimentally verified.

This successfully meets the final goal of lifetime engineering to achieve an optimal cavity. In conclusion, it has been demonstrated that for competitive $\bar{\beta}$ and $\mathrm{FOM}_2$, it is possible to also have a larger $\mathrm{FOM}_1$ value than the designs proposed by [14, 17]. This makes the silicon 1D photonic crystal EFISH device a promising candidate for efficient second harmonic generation in integrated silicon photonics for a wide variety of applications, including photonic computing, sensing, communications, space, quantum science and engineering, and machine learning accelerators.

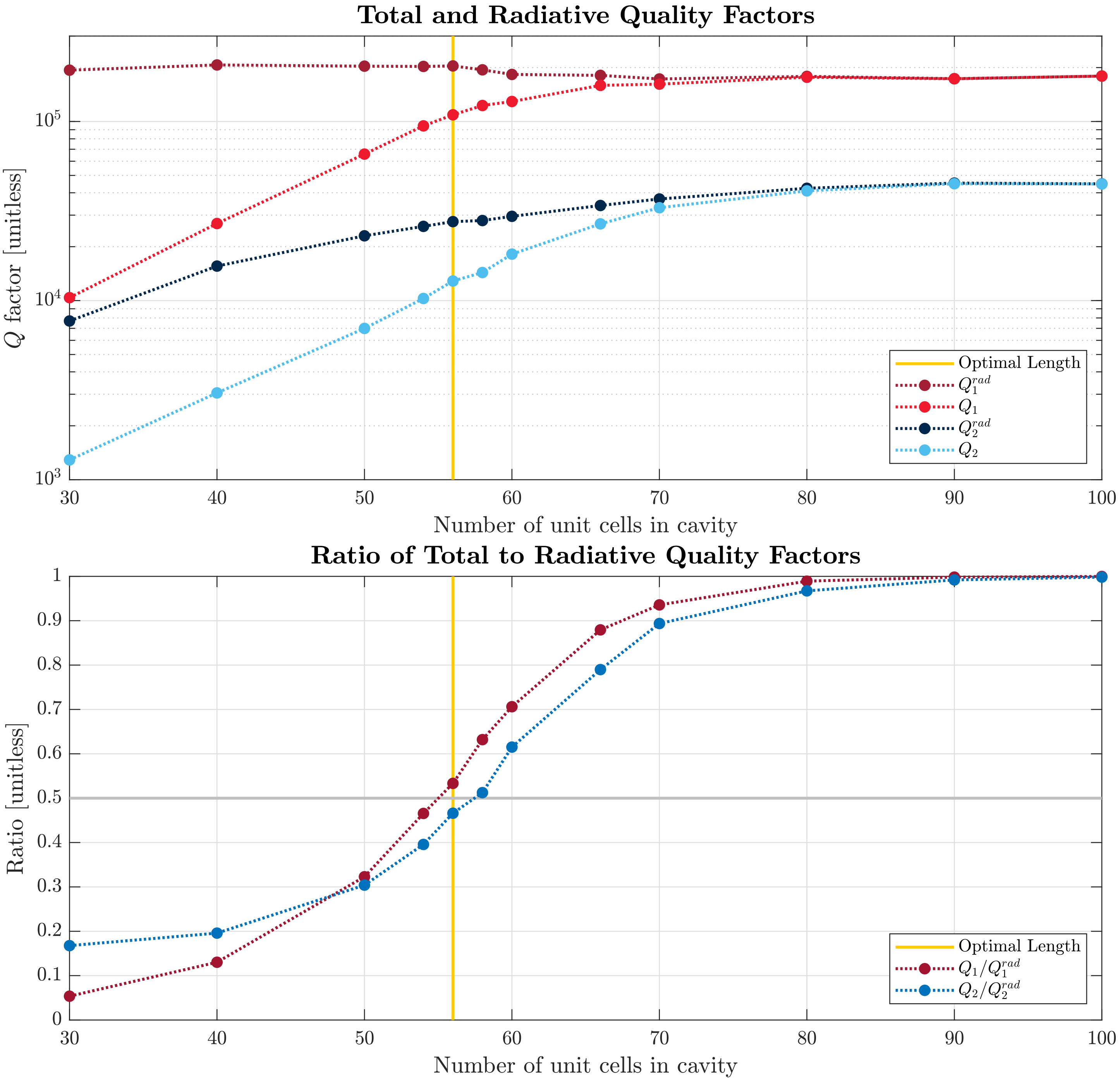

Figure 4-1: (a) *Top:* Total and radiative quality factors, and (b) *Bottom:* Ratios of total to radiative quality factors, as a function of nanobeam size for both the first and second harmonics.

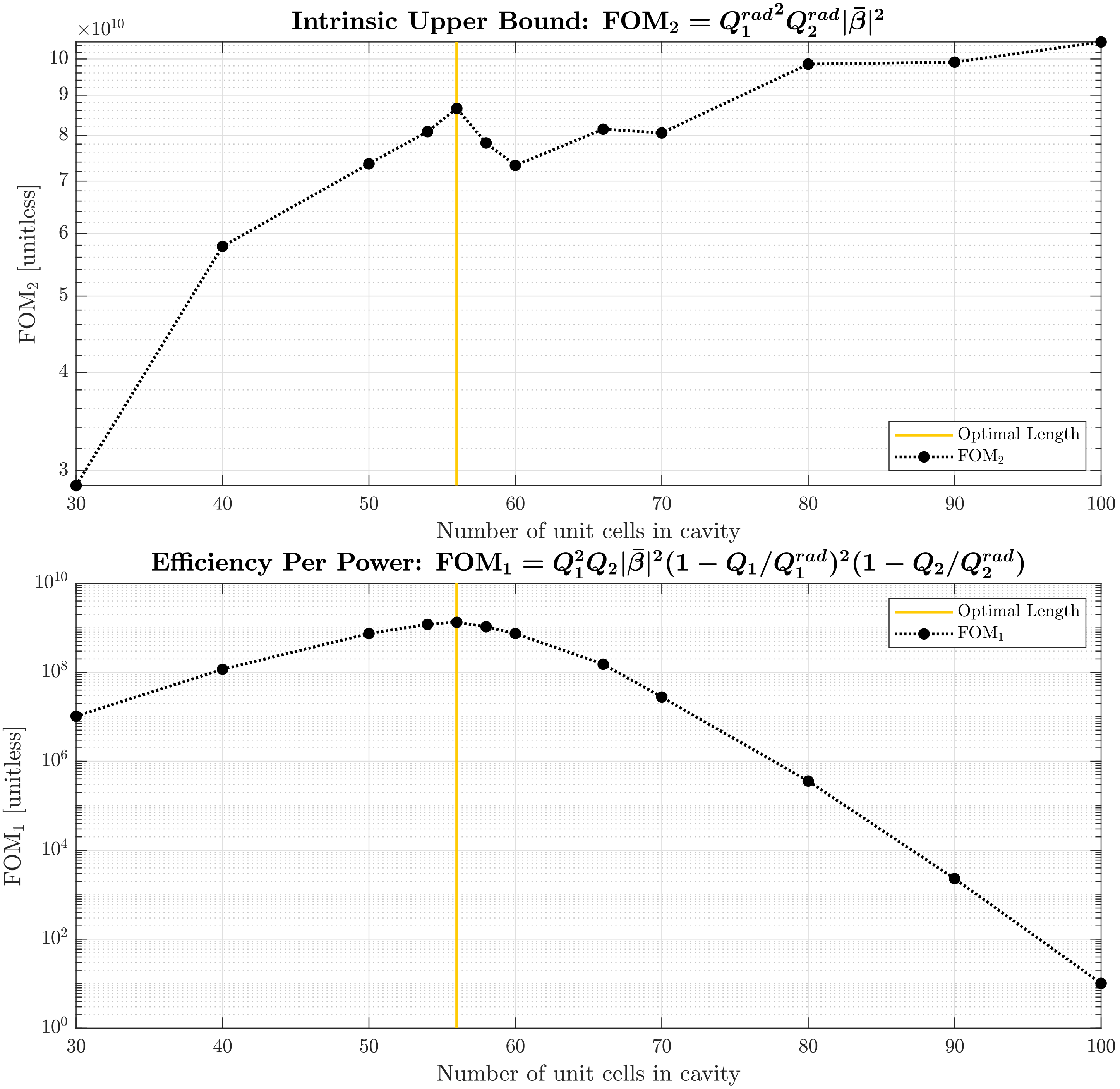

Intrinsic Upper Bound: $\mathrm{FOM}_2 = {Q_1^{rad}}^2 Q_2^{rad} |\bar{\beta}|^2$

Efficiency Per Power: $\mathrm{FOM}_1 = Q_1^2 Q_2 |\bar{\beta}|^2 (1 - Q_1/Q_1^{rad})^2 (1 - Q_2/Q_2^{rad})$

Figure 4-2: (a) *Top:* Device figure of merit 2, and (b) *Bottom:* Device figure of merit 1, as a function of nanobeam size.

# Chapter 5

# Conclusions

This thesis proposes a one dimensional photonic crystal nanobeam cavity in silicon for second harmonic generation, with high quality factors and low mode volumes for both the fundamental and second harmonic modes. Second harmonic generation in silicon is made possible by taking advantage of its electric field induced second harmonic (EFISH) effect. The unit cell's photonic crystal band structure was engineered to have same-polarization, octave-separated band gaps under the light cone. Tapering profile optimization enabled the resultant cavity to have ultralarge quality factors at both of the octave separated modes.

Consistent with Bloch's theorem, the optical field reverses sign with each unit cell, which typically leads to diminished figures of merit ($\bar{\beta}$, $\mathrm{FOM}_1$, $\mathrm{FOM}_2$) in devices relying on the intrinsic $\chi^{(2)}$ of non-centrosymmetric materials such as gallium arsenide or lithium niobate. The silicon microcavity bypasses this issue since its second-order nonlinearity is induced by an electric field whose direction can be controlled via electrode biasing. A spatially alternating DC electric field sets up a corresponding spatially alternating $\chi^{(2)}_{induced}$ that enables each unit cell to contribute positively to $\bar{\beta}$, resulting in a $\bar{\beta}$ that is an order of magnitude larger than previously obtained with gallium arsenide.

The electrode bias voltages could be realized in practice by using doped silicon. Table 5.1 lists the silicon effective second order nonlinearity for the 1 V applied in this work and estimates the voltages required for realizing the maximum induced nonlinearity possible in this design, which is limited by the silicon breakdown voltage of 40V/$\mu$m [30].

| $\boldsymbol{V_{applied}}$ | $\boldsymbol{E^{max}_{dc,y}}$ | $\overline{\boldsymbol{\chi}}^{\mathbf{(2)}}_{\text{effective}}$ | $\boldsymbol{E^{eff}_{dc,y}}$ |
|---:|---|:---:|---|
| 1 V | $4.814\ \frac{\text{mV}}{\mu\text{m}}$ | $6.012 \times 10^{-4}\ \frac{\text{pm}}{\text{V}}$ | $0.818\ \frac{\text{mV}}{\mu\text{m}}$ |
| 8.3 kV | $40.00\ \frac{\text{V}}{\mu\text{m}}$ | $4.995\ \frac{\text{pm}}{\text{V}}$ | $6.796\ \frac{\text{V}}{\mu\text{m}}$ |
| 48.9 kV | $235.4\ \frac{\text{V}}{\mu\text{m}}$ | $29.40\ \frac{\text{pm}}{\text{V}}$ | $40.00\ \frac{\text{V}}{\mu\text{m}}$ |

Table 5.1: Estimates of effective second-order nonlinearities achievable with different applied electrode bias voltages. $E^{eff}_{dc,y}$ is estimated using $\overline{\chi}^{(2)}_{\text{effective}} = 3\chi^{(3)}E^{eff}_{dc,y}$.

One avenue for future work is to design a different spatially alternating biasing profile that has a smaller difference between the maximum electric field $E^{max}_{dc,y}$ and the effective electric field for induced second harmonic generation, $E^{eff}_{dc,y}$, where $\overline{\chi}^{(2)}_{\text{effective}} = 3\chi^{(3)}E^{eff}_{dc,y}$. Another interesting boulevard is to investigate time-varying second harmonic generation in the microcavity by changing the bias voltage of the electrodes in real time.

Moreover, the $x-$spacing between adjacent electrodes causes a field between the electrodes that is on the order of the breakdown voltage of air. The addition of a dielectric into a region with some electric field will reduce the electric field in that region due to the electrostatic polarization arising in the dielectric medium. Thus, it could be advantageous to surround the electrodes with electrolytes. This would require re-engineering of the unit cell to return the second harmonic bands below the light line.

While the induced second harmonic generation values and spatial pattern are programmable with electrode bias voltage, the unit cell still has its bandgap at specific frequencies. Once the lattice constant, or unit cell length, is chosen, the physical band edge frequencies are locked in place. Additionally, once the cavity and defect design are determined, the mode inside of each bandgap is fixed at its resonant frequency, which is not conducive to tunability. Consequently, a useful direction of development is to enable tunable first- and second-harmonic wavelengths, perhaps by strain or thermal tuning.

Silicon is a scalable platform for photonics, and this work opens the door to extending these devices to nonlinear optical functions without requiring the use of additional materials.

THIS PAGE INTENTIONALLY LEFT BLANK

# Bibliography

[1] Mikkel Heuck, Kurt Jacobs, and Dirk R. Englund. "Controlled-Phase Gate Using Dynamically Coupled Cavities and Optical Nonlinearities". In: *Physical Review Letters* 124.16 (Apr. 2020). URL: `https://doi.org/10.1103/physrevlett.124.160501`.

[2] Mikkel Heuck, Kurt Jacobs, and Dirk R. Englund. "Photon-photon interactions in dynamically coupled cavities". In: *Physical Review A* 101.4 (Apr. 2020). URL: `https://doi.org/10.1103/physreva.101.042322`.

[3] Stefan Krastanov et al. "Room-temperature photonic logical qubits via second-order nonlinearities". In: *Nature Communications* 12.1 (Jan. 2021). URL: `https://doi.org/10.1038/s41467-020-20417-4`.

[4] Stefan Krastanov et al. "Controlled-phase gate by dynamic coupling of photons to a two-level emitter". In: *npj Quantum Information* 8.1 (Sept. 2022). URL: `https://doi.org/10.1038/s41534-022-00604-5`.

[5] Jasvith Raj Basani et al. *All-Photonic Artificial Neural Network Processor Via Non-linear Optics*. 2022. URL: `https://arxiv.org/abs/2205.08608`.

[6] Mikkel Heuck, Philip Trøst Kristensen, and Jesper Mørk. "Energy-bandwidth trade-off in all-optical photonic crystal microcavity switches". In: *Optics Express* 19.19 (Sept. 2011). URL: `https://doi.org/10.1364/oe.19.018410`.

[7] Mikkel Heuck et al. "Improved switching using Fano resonances in photonic crystal structures". In: *Optics Letters* 38.14 (July 2013). URL: `https://doi.org/10.1364/ol.38.002466`.

[8] Mikkel Heuck, Philip Trøst Kristensen, and Jesper Mørk. "Dual-resonances approach to broadband cavity-assisted optical signal processing beyond the carrier relaxation rate". In: *Optics Letters* 39.11 (May 2014). URL: `https://doi.org/10.1364/ol.39.003189`.

[9] E. Timurdogan et al. "Electric field-induced second-order nonlinear optical effects in silicon waveguides". In: *Nature Photonics* 11.3 (Feb. 2017). URL: `https://doi.org/10.1038/nphoton.2017.14`.

[10] Uttara Chakraborty et al. "Cryogenic operation of silicon photonic modulators based on the DC Kerr effect". In: *Optica* 7.10 (Oct. 2020). URL: `https://doi.org/10.1364/optica.403178`.

[11] Robert W. Boyd. *Nonlinear Optics*. Elsevier, 2020. URL: `https://doi.org/10.1016/c2015-0-05510-1`.

[12] Michael Hollenbach et al. "Wafer-scale nanofabrication of telecom single-photon emitters in silicon". In: *Nature Communications* 13.1 (Dec. 2022). URL: `https://doi.org/10.1038/s41467-022-35051-5`.

[13] Alex Widhalm et al. "Electric-field-induced second harmonic generation in silicon dioxide". In: *Optics Express* 30.4 (Feb. 2022). URL: `https://doi.org/10.1364/oe.443489`.

[14] Zin Lin et al. "Cavity-enhanced second-harmonic generation via nonlinear-overlap optimization". In: *Optica* 3.3 (Mar. 2016). URL: `https://doi.org/10.1364/optica.3.000233`.

[15] John D. Joannopoulos et al. *Photonic Crystals*. Princeton University Press, Oct. 2011. URL: `https://doi.org/10.2307/j.ctvcm4gz9`.

[16] Pochi Yeh. *Optical Waves in Layered Media*. Wiley, Mar. 2005. URL: `https://www.wiley.com/en-us/Optical+Waves+in+Layered+Media-p-9780471731924`.

[17] Sonia Buckley et al. "Multimode nanobeam cavities for nonlinear optics: high quality resonances separated by an octave". In: *Optics Express* 22.22 (Oct. 2014). URL: `https://doi.org/10.1364/oe.22.026498`.

[18] Hamed Saghaei, Payam Elyasi, and Bhavin J. Shastri. "Sinusoidal and rectangular Bragg grating filters: Design, fabrication, and comparative analysis". In: *Journal of Applied Physics* 132.6 (Aug. 2022). URL: `https://doi.org/10.1063/5.0098923`.

[19] Jesús Pérez-Ríos, May E Kim, and Chen-Lung Hung. "Ultracold molecule assembly with photonic crystals". In: *New Journal of Physics* 19.12 (Dec. 2017). URL: `https://doi.org/10.1088/1367-2630/aa9b49`.

[20] Ashutosh Rao et al. "Second-harmonic generation in single-mode integrated waveguides based on mode-shape modulation". In: *Applied Physics Letters* 110.11 (Mar. 2017). URL: `https://doi.org/10.1063/1.4978696`.

[21] *MPB: MIT Photonic Bands Documentation.* Accessed: 2022-12-31. URL: `https://mpb.readthedocs.io/en/latest/`.

[22] Mikkel Heuck. "All-Optical Switching in Photonic Crystal Cavities". English. PhD thesis. Technical University of Denmark, Mar. 2013. URL: `https://orbit.dtu.dk/en/publications/all-optical-switching-in-photonic-crystal-cavities`.

[23] *RefractiveIndex.Info: Optical constants of Si (Silicon) Mikhail Polyanskiy.* Accessed: 2022-12-31. URL: `https://refractiveindex.info/?shelf=main&book=Si&page=Li-293K`.

[24] Qimin Quan, Parag B. Deotare, and Marko Loncar. "Photonic crystal nanobeam cavity strongly coupled to the feeding waveguide". In: *Applied Physics Letters* 96.20 (May 2010). URL: `https://doi.org/10.1063/1.3429125`.

[25] Yoshihiro Akahane et al. “High-Q photonic nanocavity in a two-dimensional photonic crystal”. In: *Nature* 425.6961 (Oct. 2003). URL: `https://doi.org/10.1038/nature02063`.

[26] Qimin Quan and Marko Loncar. “Deterministic design of wavelength scale, ultra-high Q photonic crystal nanobeam cavities”. In: *Optics Express* 19.19 (Sept. 2011). URL: `https://doi.org/10.1364/oe.19.018529`.

[27] *Selecting the best mesh refinement option in the FDTD simulation object*. Accessed: 2022-12-31. URL: `https://optics.ansys.com/hc/en-us/articles/360034382614`.

[28] *PML boundary conditions in FDTD and MODE*. Accessed: 2022-12-31. URL: `https://optics.ansys.com/hc/en-us/articles/360034382674`.

[29] *Quality factor calculations for a resonant cavity*. Accessed: 2022-12-31. URL: `https://optics.ansys.com/hc/en-us/articles/360041611774`.

[30] R. Soref and B. Bennett. “Electrooptical effects in silicon”. In: *IEEE Journal of Quantum Electronics* 23.1 (Jan. 1987). URL: `https://doi.org/10.1109/jqe.1987.1073206`.